

# Co-rotating twin-screw extruders: Detailed analysis of conveying elements based on smoothed particle hydrodynamics. Part 1: Hydrodynamics

Andreas Eitzlmayr<sup>a</sup>, Johannes Khinast<sup>a,b,\*</sup>

<sup>a</sup> Institute for Process and Particle Engineering, Graz University of Technology, Inffeldgasse 13, 8010 Graz, Austria

<sup>b</sup> Research Center Pharmaceutical Engineering, Inffeldgasse 13, 8010 Graz, Austria

## HIGHLIGHTS

- We applied SPH to study the flow in a co-rotating twin-screw extruder.
- A new model which accounts for the flow in unresolved clearances was presented.
- We showed detailed results for pressure drop, flow rate and power consumption.
- We achieved excellent agreement with CFD data for the completely filled state.
- Detailed results for the partially filled state are included.

## ARTICLE INFO

### Article history:

Received 5 November 2014

Received in revised form

15 April 2015

Accepted 23 April 2015

Available online 20 May 2015

### Keywords:

Smoothed particle hydrodynamics

SPH

Co-rotating twin-screw extruder

Complex geometry

Partially filled

Flow

## ABSTRACT

Due to the complex geometry of the rotating screws and, typically, free surface flows in partially filled screw sections, first principles simulations of the flow in co-rotating intermeshing twin-screw extruders using the well-established, mesh-based CFD (computational fluid dynamics) approaches are highly challenging. These issues can be resolved via the smoothed particle hydrodynamics (SPH) method thanks to its meshless nature and the inherent capability to simulate free surface flows. In our previous work, we developed a novel method for modeling the boundary conditions with complex wall geometries, under which SPH could be efficiently applied to complex surfaces of typical screw geometries of extruders. In this work, we employed SPH and our boundary method to study the flow in a conveying element in detail. To address unresolved clearances, we developed a new model that is coupled to SPH and can correctly account for the flow through unresolved clearances. A validation of our approach using CFD data from the literature for a completely filled conveying element indicated excellent agreement. Consequently, we studied the flow in a partially filled conveying element and obtained results for the flow rate, the power input and the axial force with variable filling ratio. A detailed analysis of the corresponding mixing phenomena is presented in Part 2. Our results show that the proposed method is a comprehensive approach to study the flow in different types of screw elements in detail, providing an excellent basis for further development of simplified models of entire extrusion processes.

© 2015 Elsevier Ltd. All rights reserved.

## 1. Introduction

Developed in the 1940s and 1950s, intermeshing extruders have been widely used in different industries for many decades, for

example, to manufacture polymers, chemicals and foodstuffs. The most common type is the co-rotating, intermeshing twin-screw extruder. Its advantages include good mixing performance, self-cleaning screws, short residence time and good product quality. Single-screw extruders are primarily used for melting and pressure build-up and do not have superior mixing properties. Other types of extruders, such as counter-rotating twin-screw, multi-screw or ram extruders, are designed for more specialized applications. (Kohlgrüber, 2008)

In recent years, extrusion has become increasingly attractive to the pharmaceutical industry with regard to manufacturing of solid drug products (Ghebre-Sellassie and Martin, 2003). Depending on the materials involved, there are several types of pharmaceutical

*Abbreviations:* 1D, one-dimensional; 3D, three-dimensional; CAD, computer aided design; CFL, Courant–Friedrichs–Lewy; FEM, finite element method; FVM, finite volume method; SPH, smoothed particle hydrodynamics; STL, surface tessellation language

\* Corresponding author at: Institute for Process and Particle Engineering, Graz University of Technology, Inffeldgasse 13, 8010 Graz, Austria.

Tel.: +43 316 873 30400.

E-mail address: [khinast@tugraz.at](mailto:khinast@tugraz.at) (J. Khinast).

<http://dx.doi.org/10.1016/j.ces.2015.04.055>

0009-2509/© 2015 Elsevier Ltd. All rights reserved.

extrusion processes, such as hot melt extrusion (HME), hot melt granulation, wet extrusion and solid lipid extrusion (Kleinebudde, 2011). HME is particularly promising for pharmaceutical applications in terms of increasing the bioavailability of poorly soluble drug molecules and forming solid solutions and amorphous solid dispersions (Breitenbach, 2002; Repka et al., 2005). Moreover, since HME is solvent-free, it does not involve costs associated with the solvent, separation, recovery and disposal. Due to its variety of individual screw elements (e.g., conveying elements, kneading elements and mixing elements), the typical modular screw design of co-rotating, intermeshing twin-screw extruders offers almost unlimited options with regard to the actual screw configuration design. Although this allows high operational flexibility, developing an appropriate screw configuration to accommodate the actual process requirements is highly challenging and normally requires extensive experience and/or experimental and empirical work.

In experiments, an extruder is essentially a black box, and accurate measurements of process variables such as the filling ratio and the melt temperature are difficult to achieve. Modeling and simulation methods can provide an understanding of the complex flow and mixing phenomena associated with the interaction between the rotating screw geometry, material properties and operation conditions, potentially leading to effective scale-up approaches.

However, extruders are highly complex, witnessed by the fact that no fully-resolved first-principles simulations of entire twin-screw extruders have been reported to date. There are several reasons: first, free-surface flows, which are difficult to model, occur in the partially filled screw sections. Second, the flow behavior of the processed material mixtures is typically complex, mostly non-Newtonian, which requires an extensive amount of measurements for a complete description of the macroscopic properties of the material mixtures. Third, extruders are highly non-isothermal, requiring the coupling between mass, momentum and energy balances. Fourth, due to the small gap between the screws and between the screws and the barrel, the flow needs to be highly resolved. Moreover, a fully resolved simulation of the transition from the granular to the molten state is currently infeasible.

Several simulation approaches for twin-screw extruders exist today, which are mainly divided into one-dimensional (1D) and three-dimensional (3D) methods. The computationally less expensive 1D approach yields an approximate description of the process variables along the screw axes (e.g., filling ratio, pressure, and temperature) while neglecting their distributions in radial and azimuthal direction. Here, the flow around the screw geometry is not fully resolved, thus, the 1D approach depends on simplified models (based on first principles), which account for the impact of the actual screw geometry by correlating integral properties of the flow field (for example the flow rate, the axial pressure gradient or the power input). This usually involves parameters which are characteristic for the considered screw element geometries. For specific types of screw elements (e.g., conveying elements) these parameters can be determined based on analytical equations. Beyond that, the characteristic screw parameters can also be determined by experiments or fully resolved simulations, which can particularly be important for complex (real) materials and more complex geometries. Since the averaging over the cross section involves also the spatial distribution of material properties, e.g., the viscosity, the characteristic screw parameters can also depend on the considered material. However, this simplified method often yields sufficiently accurate predictions that contribute to process understanding and significantly reduce experimental effort. Due to its comparably low computational expense, it is still the only way to develop a simulation of the entire extrusion process. For more detailed information about 1D modeling, please refer to the literature, e.g., (White and Chen, 1994; Potente and

Hanhart, 1994; Vergnes et al., 1998; Potente et al., 1999; White et al., 2001; Potente and Kretschmer, 2002; Prat et al., 2002; Choulak et al., 2004; Vergnes and Berzin, 2006; Bahloul et al., 2011; Teixeira et al., 2012; Eitzlmayr et al., 2014b).

For first principles simulations of the flow in co-rotating twin-screw extruders, mainly mesh-based CFD (computational fluid dynamics) methods, such as the FEM (finite element method) and FVM (finite volume method), have been used (e.g., Ishikawa, 2001; Bertrand et al., 2003; Malik and Kalyon, 2005; Ficarella et al., 2006a; Ficarella et al., 2006b; Kalyon and Malik, 2007; Barrera et al., 2008; Bierdel, 2008; Conzen, 2008; Rodríguez, 2009; Haghighyeghi et al., 2010; Vyakaranam et al., 2012; Sarhangi Fard et al., 2012a; Sarhangi Fard et al., 2012b; Sarhangi Fard and Anderson, 2013; Héty and Ilinca, 2013; Rathod and Kokini, 2013; Sobhani et al., 2013; Durin et al., 2014). FEM was also used to simulate complex fluids in extruders including wall slip phenomena, (e.g., Kalyon et al., 1999; Lawal et al., 1999; Malik et al., 2014). However, simulating free-surface flows in partially filled screw sections remains extremely challenging. To address this issue, Pokriefke (2005), for example, used FVM with an Eulerian multiphase model and applied a sophisticated mesh refinement at the free surfaces.

Being mesh-free, the smoothed particle hydrodynamics (SPH) method may be used to simulate partially filled extruders: achieving partial filling requires the same effort as complete filling and mixing phenomena can be observed by tracking tracer particles without additional modeling work. Cleary and Robinson (2011) applied SPH to study mixing in a co-rotating twin-screw extruder using boundary particles to model the screw and barrel surfaces.

In this work, we applied SPH to study the hydrodynamics (Part 1) and mixing (Part 2) in a conveying element of a co-rotating twin-screw extruder in completely- and partially-filled states. For the boundary conditions at the wall surfaces, we used a new approach proposed in our previous work (Eitzlmayr et al., 2014a). Instead of the classical method of modeling walls in SPH based on particles (e.g., boundary particles and ghost particles), we determined polynomial fits to calculate the interaction of a solid wall with adjacent fluid particles directly from the distances between the wall and the fluid particles. This can be efficiently applied to complex geometries in the STL (surface tessellation language) format generated by commonly used CAD (computer aided design) software and, thus, allows a practicable pre-processing strategy for complex geometries in SPH simulations.

## 2. Dimensionless groups

Pawlowski (1971) introduced dimensionless groups to describe the flow in screw machines and, specifically, single-screw extruders. Kohlgrüber (2008) applied them to twin-screw extruders based on the assumption that the relevant flow parameters of a completely filled screw element were the barrel diameter  $D$  as the measure of the length scale, the fluid viscosity  $\eta$ , the fluid density  $\rho$ , the screw speed  $n$ , the achieved flow rate  $\dot{V}$ , the axial pressure drop  $\Delta p$  over the considered length  $L$ , the screw driving power  $P$  and the axial force  $F$  exerted on the screws. By means of dimensional analysis, these nine parameters can be reduced to six dimensionless groups. One of them is the simplex  $L/D$ , which is usually neglected by considering an infinitely extended system ( $L/D \rightarrow \infty$ ). The remaining five dimensionless groups are the Reynolds number  $Re = nD^2\rho/\eta$ , the dimensionless flow rate  $\dot{V}/nD^3$ , which can be viewed as throughput per screw revolution (using the screw speed  $n$ ) relative to the volume of the extruder (represented by the cubed barrel diameter  $D$ ), the dimensionless axial pressure drop  $\Delta p D / \eta n L$  (based on viscosity  $\eta$  and the

axial length  $L$ ), the dimensionless driving power  $P/\eta n^2 D^2 L$  and the dimensionless axial force  $F/\eta n D L$ .

As shown theoretically and experimentally (Pawlowski, 1971; Kohlgrüber, 2008), the flow in a completely filled screw element (single- or twin-screw) can be described via correlations of the dimensionless groups: the so-called pressure characteristic  $\Delta p D / \eta n L = f_A(Re, \dot{V} / n D^3)$ , the power characteristic  $P / \eta n^2 D^2 L = f_B(Re, \dot{V} / n D^3)$  and the axial force characteristic  $F / \eta n D L = f_C(Re, \dot{V} / n D^3)$ . For creeping flows ( $Re \rightarrow 0$ ), which usually occur in extruders due to the high viscosities, the dependency on the Reynolds number vanishes. Thus, for the specific case of a Newtonian temperature-independent fluid under the creeping flow conditions these correlations are characteristic for the geometry of the considered screw element in the dimensionless form (as they do not depend on the length scale, viscosity and screw speed). Moreover, in this case, the correlations are linear due to the linearity of the Stokes equations valid for creeping flows. Then they can be described by the axis intercepts of the power characteristic ( $A_1$ ,  $A_2$ ), pressure characteristic ( $B_1$ ,  $B_2$ ) and axial force characteristic ( $C_1$ ,  $C_2$ ) (Pawlowski, 1971; Kohlgrüber, 2008):

$$\frac{\Delta p D}{\eta n L} = A_2 \cdot \left( 1 - \frac{1}{A_1} \frac{\dot{V}}{n D^3} \right) \quad (1)$$

$$\frac{P}{\eta n^2 D^2 L} = B_2 \cdot \left( 1 - \frac{1}{B_1} \frac{\dot{V}}{n D^3} \right) \quad (2)$$

$$\frac{F}{\eta n D L} = C_2 \cdot \left( 1 - \frac{1}{C_1} \frac{\dot{V}}{n D^3} \right) \quad (3)$$

Specifically, parameter  $A_1$  represents the dimensionless flow rate in a completely filled screw element without backpressure, which is termed “inherent conveying capacity”. Similarly, the parameters  $B_1$  and  $C_1$  are the dimensionless flow rates at zero driving power and zero axial force, which are less relevant for practical applications. The parameters  $A_2$ ,  $B_2$  and  $C_2$  represent the dimensionless pressure drop, driving power and axial force at zero flow rate, i.e., when conveying against a closed die.

### 3. Reference case and geometry

To validate the results of the SPH simulation, we used the results of FVM simulations of a two-flighted conveying element of a co-rotating twin-screw extruder in the completely filled state reported by Bierdel (2008), who specifically described the pressure characteristic (Eq. (1)) and the power characteristic (Eq. (2)) of this element. The geometry is illustrated in Fig. 1. The outer screw diameter is  $D_o = 60$  mm, the inner screw diameter is  $D_i = 38$  mm, the centerline distance is  $C = 50$  mm and the barrel diameter is  $D = 61$  mm (thus, the clearance distances are 0.5 mm between the screw and the barrel and 1 mm between the screws). The pitch is  $T_s = 120$  mm, the length is half of the pitch ( $L = 60$  mm) and periodic boundaries were applied in the  $z$ -direction.

From these data, we modeled the screw geometry using the software SolidWorks according to the definition of the cross section profile of closely intermeshing twin-screw extruders (see e.g., Kohlgrüber, 2008; Booy, 1978; Rauwendaal, 2001). However, since only the fully wiped geometry (i.e., without clearances) is exactly defined by the underlying kinematic principles, additional strategies are required to construct the clearances. Since this specific detail was not obvious from (Bierdel, 2008), we used the simplest method and generated the clearances by increasing the centerline distance and the barrel diameter, i.e., by constructing the fully-wiped profile with a centerline distance  $C = 49$  mm and a barrel diameter  $D = 60$  mm, subsequently shifting the screws in the radial direction by 1 mm and increasing the barrel diameter by 1 mm to achieve the clearances. The resulting geometry A is shown in Fig. 1.

To import the geometry into the simulation software LIGGGTHS, we converted the screw and barrel geometry into the STL format with the open-source tool GMSH (<http://geuz.org/gmsh/>), approximating the spatially curved surfaces with small triangles (see Fig. 2).

In order to investigate the effect of the clearances on the simulation results, we performed simulations in a modified geometry, with closed clearances between the screws and the barrel, i.

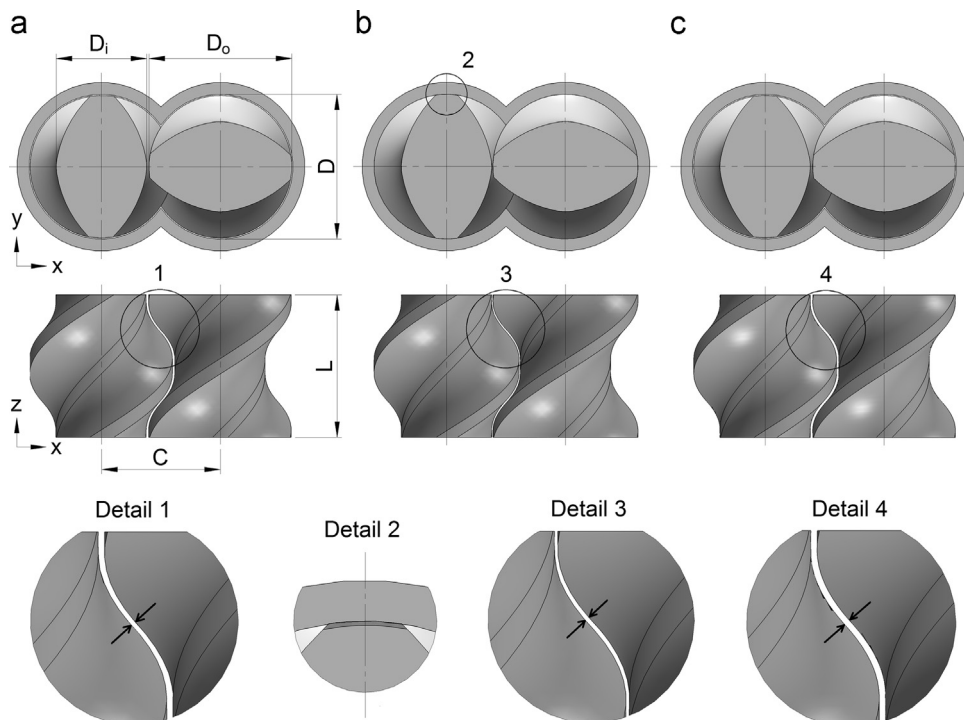


Fig. 1. Geometry of the two-flighted conveying element and details of the clearances.

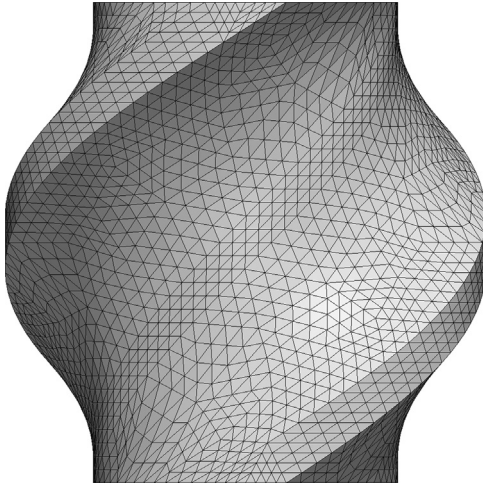


Fig. 2. STL surface mesh of the screw element.

e., the outer screw diameter  $D_o$  was equal to the barrel diameter  $D$ . For that purpose, we extended the screw flights of geometry A by 0.5 mm, as shown by the dark shaded area in Fig. 1, Detail 2. This yielded the geometry B. Detail 3 in Fig. 1 illustrates that the clearance between the screws is halved compared to Detail 1.

However, we later learned from personal communication that Bierdel (2008) used a different method to create the clearances, the so-called “surface-equidistant method” constructing the fully-wiped profile with the final values of  $C=50$  mm and  $D=61$  mm and, subsequently, offsetting the surface of the screw element by 0.5 mm perpendicularly to the surface.

A screw geometry based on the surface-equidistant method yields a constant clearance distance in the intermeshing region, i. e., avoids tighter clearances between the screws at small pitches (and the corresponding high shear conditions). Clearly, this has advantages, particularly with regard to sensitive materials. However, in contrast to other methods (Kohlgrüber, 2008), the resulting cross section profile depends on the pitch of the screw element, leading to a slight mismatch at the interface of various screw elements. As such, the extruder manufacturers typically do not use the surface-equidistant method.

Geometry C, resulting from the surface equidistant method and shown in Fig. 1, was almost equal to geometry A, with the identical main dimensions  $D$ ,  $C$ ,  $D_o$  and  $D_i$ . However, the surface-equidistant method yielded a slightly different cross-sectional profile of geometry C, and the clearances between the screws were slightly increased in some regions compared to geometry A (illustrated in Fig. 1, Details 1 and 4). Therefore, we repeated two of our simulations with geometry C to determine how this affected the agreement with the data of (Bierdel, 2008).

## 4. Computational approach

### 4.1. Smoothed particle hydrodynamics (SPH)

The SPH method is a Lagrangian particle method, where the fluid is discretized into small mass points (so-called particles). The flow is represented by the movement of those particles, which is calculated based on interaction forces approximating the continuity and momentum equations.

We used the weakly compressible SPH method according to Monaghan (e.g., Monaghan, 1992; Monaghan, 1994; Monaghan, 2000; Monaghan, 2005), calculating the density via the discretized

continuity equation:

$$\frac{d\rho_a}{dt} = \sum_b m_b (\vec{v}_a - \vec{v}_b) \cdot \vec{\nabla}_a W_{ab} \quad (4)$$

where  $m$  is the particle mass,  $\vec{v}$  is the particle velocity and  $\vec{\nabla}_a W_{ab}$  is the gradient of the kernel function  $W$  around particle  $b$  evaluated at in the position of particle  $a$ . For the momentum equation, we used the form proposed by Morris et al. (1997) for low-Reynolds-number flows. In addition, we applied the tensile correction  $R(f_{ab})^4$  of Monaghan (2000):

$$\begin{aligned} \frac{d\vec{v}_a}{dt} = & - \sum_b m_b \left( \frac{p_a}{\rho_a^2} + \frac{p_b}{\rho_b^2} + R(f_{ab})^4 \right) \vec{\nabla}_a W_{ab} \\ & + \sum_b \frac{m_b (\eta_a + \eta_b)}{\rho_a \rho_b} \left( \frac{1}{|\vec{r}_{ab}|} \frac{\partial W_{ab}}{\partial r_{ab}} \right) \vec{v}_{ab} + \vec{a}, \end{aligned} \quad (5)$$

where  $p$  is the pressure,  $\eta$  the dynamic viscosity,  $\vec{r}_{ab} = \vec{r}_a - \vec{r}_b$  is the distance vector between particles  $a$  and  $b$ ,  $\vec{v}_{ab} = \vec{v}_a - \vec{v}_b$  is the relative velocity and  $\vec{a}$  is a body force (e.g., gravity). The tensile correction  $R(f_{ab})^4$  (Monaghan, 2000) is an artificial term, which is required to avoid the unphysical clustering of fluid particles at low pressures that may occur at free surfaces. All other terms in Eq. (5) represent physical forces, i.e., the pressure forces, viscous forces and body forces. The factor  $f_{ab}$  of the tensile correction is defined as:

$$f_{ab} = \frac{W_{ab}}{W(\Delta x, h)} \quad (6)$$

The factor  $R$  consists of two contributions, one for each of the considered fluid particles  $a$  and  $b$ :

$$R = R_a + R_b \quad (7)$$

where  $R_a$  is calculated by:

$$R_a = \begin{cases} \frac{\varepsilon |p_a|}{\rho_a^2} & (p_a < 0) \\ 0 & (\text{otherwise}) \end{cases} \quad (8)$$

$R_b$  is obtained analogous to  $R_a$  by replacing  $a$  with  $b$ , the parameter  $\varepsilon$  is commonly set to 0.2. If both pressures  $p_a$  and  $p_b$  are positive, Monaghan (2000) recommends to calculate  $R$  as follows:

$$R = 0.01 \left( \frac{p_a}{\rho_a^2} + \frac{p_b}{\rho_b^2} \right) \quad (9)$$

Similarly to our previous work (Eitzlmayr et al., 2014a), we used the following linear form for the equation of state to approximate an incompressible fluid:

$$p = c^2 (\rho - \rho_0) + p_0 \quad (10)$$

where  $c$  is the speed of sound in the fluid,  $\rho_0$  is the reference density and  $p_0$  is a background pressure (Adami et al., 2013). The chosen speed of sound had to be high enough to keep the density variability low in the case of liquids (typically  $\delta = \Delta\rho/\rho_0 \leq 0.01$ ). The criteria to achieve this are described in Morris et al. (1997):

$$c^2 \geq \frac{1}{\delta} \max \left( V_0^2, \frac{\nu V_0}{L_0}, a L_0 \right), \quad (11)$$

where  $V_0$  is the maximum fluid velocity,  $\nu$  is the kinematic fluid viscosity,  $L_0$  is a relevant length scale and  $a$  is a body force acting on the particles. The first criterion limits the compression due to kinetic energy and can also be expressed by the Mach number ( $Ma^2 \leq \delta$ , see also Monaghan (1994)). The second and third criteria in Eq. (11) limit the compression due to the viscous and body forces.

We filtered the density field every 30th time steps using the Shepard correction (e.g., Gomez-Gesteira et al. (2010)), which is a common way of avoiding unphysical oscillations in the pressure



field caused by small density errors that typically accumulate over time due to Eq. (4):

$$\rho_a^{\text{new}} = \frac{\sum_b m_b W_{ab}}{\sum_b \frac{m_b}{\rho_b} W_{ab}} \quad (12)$$

For the kernel function  $W$ , we employed the cubic-spline kernel defined as follows (Monaghan, 2000):

$$W\left(\left|\vec{r}_{ab}\right|, h\right) = \frac{1}{\pi h^3} \begin{cases} 1 - \frac{3}{2} \left(\frac{\left|\vec{r}_{ab}\right|}{h}\right)^2 + \frac{3}{4} \left(\frac{\left|\vec{r}_{ab}\right|}{h}\right)^3 & 0 \leq \frac{\left|\vec{r}_{ab}\right|}{h} < 1 \\ \frac{1}{4} \left(2 - \frac{\left|\vec{r}_{ab}\right|}{h}\right)^3 & 1 \leq \frac{\left|\vec{r}_{ab}\right|}{h} < 2 \\ 0 & 2 \leq \frac{\left|\vec{r}_{ab}\right|}{h} \end{cases} \quad (13)$$

The smoothing length  $h$  was set to 1.2 times particle spacing  $\Delta x$  ( $h = 1.2\Delta x$ ), resulting in a number of approximately 57 neighbors within a sphere of radius  $2h$ , as recommended in (Monaghan, 2005; Liu and Liu, 2003). Since the particle spacing develops dynamically during a simulation, we used its initial value to determine the smoothing length, at which the particles were regularly arranged on a cubic lattice. Considering that in a weakly compressible flow the density (i.e., mass per volume) is almost constant, there can be no significant changes of the average particle spacing during a simulation.

The following criteria were shown by Morris et al. (1997) to determine the required time step, which is crucial for stability ( $c$  being the speed of sound,  $a$  the body force and  $\nu$  the kinematic fluid viscosity):

$$\Delta t \leq \min\left(0.25 \frac{h}{c}, 0.125 \frac{h^2}{\nu}, 0.25 \sqrt{\frac{h}{a}}\right) \quad (14)$$

The first constraint in Eq. (14) is a Courant–Friedrichs–Lewy (CFL) condition, and the second and third ones are due to the viscous forces and body forces. Another criterion shown by Monaghan (1989) considers the CFL condition and the viscous limitation together (simplified for liquids):

$$\Delta t \leq \frac{0.3h}{c(1+1.2\alpha)} \quad (15)$$

where  $\alpha$  is the artificial viscosity, which can be calculated from the kinematic viscosity by  $\alpha = 10\nu/hc$  (Monaghan, 2005). Note that the limit of Eq. (15) for  $\alpha \rightarrow 0$  is  $\Delta t \leq 0.3 h/c$ , while in the case of  $\alpha \rightarrow \infty$  after substituting  $\alpha$  by  $10\nu/hc$  it is  $\Delta t \leq 0.025 h^2/\nu$ . These are qualitatively equivalent to the first and second criteria in Eq. (14).

For more details concerning the fundamentals of SPH, please refer to the literature (e.g., Monaghan, 1992; Monaghan, 1994; Monaghan, 2000; Monaghan, 2005; Liu and Liu, 2003; Price, 2012; Gomez-Gesteira et al., 2010). The numerical studies were conducted using the open-source particle simulator LIGGGHTS (Kloss et al., 2012).

## 4.2. Wall boundary conditions

There is still no unique way of modeling solid walls in SPH. Commonly used techniques include boundary particles, fixed fluid particles, ghost particles and normalizing conditions (Monaghan and Kajtar, 2009). Boundaries consisting of particles are problematic for complex geometries, since the creation of a regular arrangement of boundary particles along arbitrarily curved walls would require a sophisticated procedure. Moreover, technical geometries are usually available in file formats that approximate the curved surfaces by a tessellation consisting of triangles (e.g., the STL format), and a direct

use of these commonly used geometry formats would be much simpler than a pre-processing required to set boundary particles. Ghost particles, which are fluid particles mirrored over wall surfaces, lead to complications at edges and corners. Normalizing conditions are involved and computationally expensive in 3D.

However, proper wall modeling is essential in SPH, since for particles in the vicinity of the walls the number of neighbors is not complete, which causes unphysical effects. Due to the drawbacks of the existing methods for complex geometries, we developed a novel wall interaction method, which accounts for the contributions of the wall to the continuity and momentum equation of a single fluid particle, depending on the distance of the fluid particle from the wall surface. This was presented in detail in our previous work (Eitzlmayr et al., 2014a), where we used a solid wall consisting of fixed fluid particles (representing the missing neighbors) to investigate their impact on a single, moving fluid particle. The results, transformed into a dimensionless and general form, were fitted by polynomials, which allow the efficient calculation of the wall interaction terms using the distance of the fluid particle from the wall surface, without requiring any additional particles to represent the wall. For more details please refer to our previous work (Eitzlmayr et al., 2014a).

In addition to these wall contributions to the continuity and momentum equation of the fluid particles, a repulsive force was required to prevent the penetration of fluid particles into the walls in regions with strong fluid compression. For the detailed reasons, please refer to our previous work (Eitzlmayr et al., 2014a). Similar as shown there, we used the following repulsion model, which was proposed by Monaghan with  $\alpha=4$ ,  $\beta=2$  (Monaghan, 1994) and  $\alpha=1/2$ ,  $\beta=-1/2$  (Monaghan and Kos, 1999):

$$F_{\text{rep}}(r) = \begin{cases} C_{\text{rep}} \cdot \left[\left(\frac{r_0}{r}\right)^\alpha - \left(\frac{r_0}{r}\right)^\beta\right] & (r \leq r_0) \\ 0 & (r > r_0) \end{cases} \quad (16)$$

where  $r$  is the normal distance to the wall and  $r_0$  is the range of the potential. We established that the computationally less expensive exponents  $\alpha=1$ ,  $\beta=0$  not only worked well in our case, but also allowed larger time steps than  $\alpha=4$ ,  $\beta=2$ . Thus, we used Eq. (16) with  $\alpha=1$ ,  $\beta=0$ . For consistency with the considerations in (Eitzlmayr et al., 2014a), a half-particle spacing was used for the range of the repulsion force  $r_0 = \Delta x/2$ .

## 4.3. Clearance flow

### 4.3.1. Modeling

An intrinsic characteristic of the SPH method (without using variable resolution schemes) is that the resolution in the entire flow field is constant. The resolution used in this work equals one layer of fluid particles in the clearances, i.e., the average particle spacing was equal to the clearance distance (0.5 mm). Thus, the clearance flow is not fully resolved. Even in this case, about  $10^6$  SPH particles are required to fill the entire volume with the associated computational costs. A resolution refinement by factor  $\xi$  would lead to a  $\xi^3$ -fold increase in the number of particles in 3D and, together with the corresponding time step refinement, approximately to a  $\xi^4$ -fold increase in the computational expense (i.e., a refinement by factor  $\xi=5$  would lead to a 125- and about 625-fold increase in the number of particles and the computational expense, respectively).

Even applying a variable resolution SPH scheme (i.e., a local refinement by splitting and merging of particles, e.g., Feldman and Bonet, 2007; Vacondio et al., 2013) cannot solve that problem efficiently. Since the volume fraction of the clearances was about 2% for the considered geometry, the local refinement would still lead to an increase by a factor of  $0.02 \xi^4$  in the computational expense (e.g., a refinement by factor  $\xi=5$  would require a 12-fold

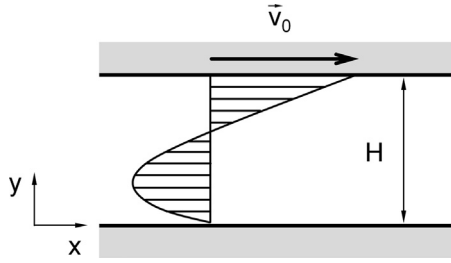


Fig. 3. Velocity profile in a channel between two parallel walls.

increase in the computational expense). The reason for this extreme ratio is that the refinement in SPH occurs equally in all directions, while it is required only in the cross-direction of the clearances. Under mesh-based CFD methods, stretched cells, which resolve the cross-direction finer than the longitudinal direction, are used in such cases. This has no equivalent in SPH.

To overcome this challenge, we proposed a model based on the analytical solution of the Newtonian flow between two parallel walls, which appropriately accounts for the flow rate and the wall shear forces in unresolved clearances. The steady and developed flow between two parallel walls in 3D (with distance  $H$  and relative velocity  $\vec{v}_0$ , as illustrated in Fig. 3) at a constant viscosity  $\eta$  with a pressure gradient  $\vec{\nabla} p$  can be easily derived from the Navier–Stokes equations. This yields the following velocity profile, which is the superposition of a linear drag flow profile over a pressure-driven, parabolic velocity profile:

$$\vec{v}(y) = \vec{v}_0 \frac{y}{H} - \frac{H^2}{2\eta} \vec{\nabla} p \left(1 - \frac{y}{H}\right) \frac{y}{H} \quad (17)$$

Note that the vectors in Eq. (17) are parallel to the walls since the velocity component normal to the walls is strictly zero. Since this velocity profile is a parabola, it is completely defined by 3 velocity vectors (i.e., the velocity of a single fluid particle in the clearance and the known wall velocities). As such, the pressure gradient  $\vec{\nabla} p$  can be calculated using Eq. (17) with the values of the relative wall velocity  $\vec{v}_0$  and the particle velocity  $\vec{v}(y)$  at the position  $y$ :

$$\vec{\nabla} p = \frac{2\eta}{(H-y)y} \left( \vec{v}_0 \frac{y}{H} - \vec{v}(y) \right) \quad (18)$$

To apply this to a fluid particle “a” in the clearance (illustrated in Fig. 4), we considered the general case of both walls moving. In this case, the velocities of fluid particle  $\vec{v}_a$  and upper wall  $\vec{v}_{W,2}$  can be formulated relative to the lower wall velocity  $\vec{v}_{W,1}$ :

$$\vec{v}_{a,rel} = \vec{v}_a - \vec{v}_{W,1} \quad (19)$$

$$\vec{v}_{W,rel} = \vec{v}_{W,2} - \vec{v}_{W,1} \quad (20)$$

Substituting  $\vec{v}(y) = \vec{v}_{a,rel}$ ,  $\vec{v}_0 = \vec{v}_{W,rel}$ ,  $y = r_1$  and  $H = r_1 + r_2$  in Eq. (18) yields:

$$\vec{\nabla} p = \frac{2\eta}{r_1 r_2} \left( \vec{v}_{W,rel} \frac{r_1}{r_1 + r_2} - \vec{v}_{a,rel} \right), \quad (21)$$

which is a measure of the curvature of the velocity profile at the position of the considered fluid particle in the clearance and can be used to calculate the corresponding wall shear stresses. To that end, the velocity gradients on both walls can be obtained from Eq. (17) by differentiation:

$$\left. \frac{d\vec{v}}{dy} \right|_{y=0} = \frac{\vec{v}_0}{H} - \frac{H}{2\eta} \vec{\nabla} p \quad (22)$$

$$\left. \frac{d\vec{v}}{dy} \right|_{y=H} = \frac{\vec{v}_0}{H} + \frac{H}{2\eta} \vec{\nabla} p \quad (23)$$

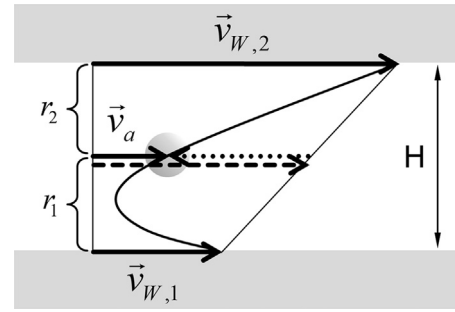


Fig. 4. Single fluid particle in a clearance with the velocity vectors of both walls and the particle. The dashed and dotted arrows show the drag flow contribution and the pressure-driven contribution of the flow, respectively. The distances  $r_1$  and  $r_2$  are the wall distances of the particle.

Multiplication with viscosity  $\eta$  and substitution of  $\vec{v}_0 = \vec{v}_{W,rel}$  and  $H = r_1 + r_2$  yield the wall shear stresses of the lower and upper walls:

$$\vec{\tau}_{W,1} = \eta \frac{\vec{v}_{W,rel}}{r_1 + r_2} - \frac{r_1 + r_2}{2} \vec{\nabla} p \quad (24)$$

$$\vec{\tau}_{W,2} = \eta \frac{\vec{v}_{W,rel}}{r_1 + r_2} + \frac{r_1 + r_2}{2} \vec{\nabla} p \quad (25)$$

To calculate the corresponding wall forces, the shear stresses are multiplied by the wall contact area. This is obtained as the fluid particle volume divided by the clearance distance (i.e., considering the volume uniformly distributed across the clearance):

$$A_{contact} = \frac{m_p}{\rho_p(r_1 + r_2)} \quad (26)$$

With that, the wall forces of the lower wall  $\vec{F}_{W,1}$  and upper wall  $\vec{F}_{W,2}$  exerted on the considered fluid particle are:

$$\vec{F}_{W,1} = -\vec{\tau}_{W,1} A_{contact} \quad (27)$$

$$\vec{F}_{W,2} = \vec{\tau}_{W,2} A_{contact} \quad (28)$$

This allows to calculate the wall shear forces in an unresolved clearance, which requires substituting the Morris viscosity model with Eqs. (19)–(21) and (24)–(28) in the momentum equation (Eq. (5)):

$$\frac{d\vec{v}_a}{dt} = - \sum_b m_b \left( \frac{p_a}{\rho_a^2} + \frac{p_b}{\rho_b^2} + R(f_{ab})^4 \right) \vec{v}_a W_{ab} + \frac{\vec{F}_{W,1} + \vec{F}_{W,2}}{m_a} + \vec{a} \quad (29)$$

However, calculating the pressure forces this way would yield too little pressure gradient contributions due to the incomplete neighbor count at positions within the clearance. Although the used wall interaction was developed to compensate the lack of neighbors in the vicinity of the walls, it fails in terms of the pressure gradients, since the wall reflects uniform pressure and does not contribute to any tangential pressure gradients. This deficiency vanishes in resolved flows since the pressure gradient is calculated correctly for all particles with a complete neighbor count (i.e., inside the fluid). However, in the most extreme case with only one layer of fluid particles across the clearance, all particles have an incomplete neighbor count and tangential pressure gradients are not correctly represented. Grenier et al. (2009) showed that the kernel gradient can be renormalized with the factor  $\Sigma(m_b/\rho_b)W_{ab}$ , which yields the value of 1 for a complete neighbor count (inside the fluid) and values  $< 1$  for an incomplete neighbor count (at boundaries). The more complex matrix renormalization proposed by Bonet and Lok (1999) would additionally guarantee the first order consistency, i.e., the exact evaluation of the gradient of a linear field. However, the

use of this technique is computationally more expensive because it requires the evaluation of nine additional neighbor summations in 3D, compared to only one summation for the scalar factor  $\sum(m_b/\rho_b)W_{ab}$ . As we found, that also the latter could reproduce pressure gradients sufficiently accurate for technical applications (see the validation cases below), we used this for the renormalization of the pressure gradient in the clearance regions. With that, the modified momentum equation for the unresolved clearance is:

$$\frac{d\vec{v}_a}{dt} = - \frac{\sum_b m_b \left( \frac{p_a}{\rho_a^2} + \frac{p_b}{\rho_b^2} + R(f_{ab})^4 \right) \vec{\nabla}_a W_{ab}}{\sum_b \frac{m_b}{\rho_b} W_{ab}} + \frac{\vec{F}_{w,1} + \vec{F}_{w,2}}{m_a} + \vec{a} \quad (30)$$

Although all forces are appropriately calculated in Eq. (30), the resulting flow rate through the clearance is typically incorrect since the entire fluid in the clearance moves together with the resulting particle velocities. For example, if the applied resolution is equal to the clearance distance  $H$  (yielding a single layer of fluid particles in the clearance), a pure Poiseuille flow causes the entire fluid in the clearance to move with the maximum velocity, while slower velocities adjacent to the walls are not accounted for.

In order to achieve a particle velocity equal to the equivalent average velocity of the flow rate (and, thus, the correct flow rate through the clearance), we introduced an appropriate velocity correction factor that was determined as follows: A pure drag flow (linear profile) does not require a velocity correction since the particle velocity is equal to the average velocity (assuming the particles are located in the center of the clearance, which is the case due to the wall symmetry). The maximum velocity of a purely pressure-driven flow (parabolic profile) is 1.5 times higher than the average velocity, i.e., without the correction the flow rate would be overestimated by 50%. Thus, the pressure-driven contribution of the superposed flow profile (see Fig. 4, dotted arrow) has to be corrected accordingly. Since in Eq. (21), exactly this pressure-driven contribution of the velocity is stated in brackets (i.e., the difference of the actual particle velocity and the drag flow contribution), we added multiplication with the velocity correction factor  $f_{corr}$  (which is 1.5 for one layer of particles in the clearance):

$$\vec{\nabla} p = \frac{2\eta}{r_1 r_2} \left( \vec{v}_{w,rel} \frac{r_1}{r_1 + r_2} - \vec{v}_{a,rel} \right) f_{corr} \quad (31)$$

As such, the  $f_{corr}$ -fold value of the pressure-driven contribution of the particle velocity is used to calculate the pressure gradient and the corresponding wall shear forces, which means that in a steady state the obtained particle velocity is equal to the flow-rate-equivalent average velocity.

Since this model should also properly account for the flow if the clearance contains more than one layer of fluid particles, the dependency of the velocity correction factor on the number of particle layers in the clearance must be considered. The number of particle layers can be calculated as the clearance distance divided by the fluid particle spacing  $N = (r_1 + r_2)/\Delta x$ . For a number of  $N$  particles layers, the average velocity of the particles  $v_{av,P}(N)$  can be calculated as

$$v_{av,P}(N) = \frac{1}{N} \sum_{i=1}^N v(y), \quad (32)$$

where  $v(y)$  is the velocity of the particle in position  $y$  in the cross-direction (see Fig. 5).

The parabolic function  $v(y)$  for a pure Poiseuille flow in 2D can be obtained from Eq. (17) (using the average velocity of the parabola  $v_{av}$ , illustrated with the dashed line in Fig. 5):

$$\frac{v(y)}{v_{av}} = 6 \left( 1 - \frac{y}{H} \right) \frac{y}{H} \quad (33)$$

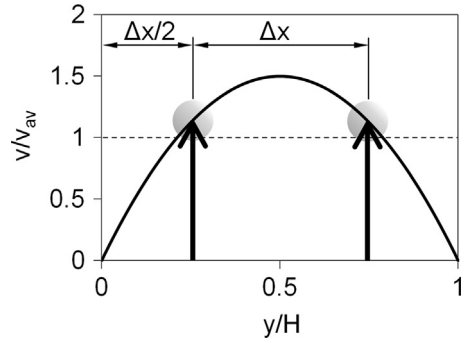


Fig. 5. Parabolic velocity profile in a pressure-driven clearance flow with, e.g., two layers of fluid particles representing the flow ( $N=2$ ). The dashed line shows the flow-rate-equivalent average velocity of the parabola  $v_{av}$ , the arrows illustrate the particle velocity vectors (without the velocity correction factor) and  $\Delta x$  is the particle spacing.

Substituting Eq. (33) in Eq. (32) and calculating the particle position of particle  $i$  as  $y = \Delta x/2 + (i-1)\Delta x$  (as illustrated in Fig. 5) using  $\Delta x/H = 1/N$  yields:

$$\frac{v_{av,P}}{v_{av}} = \frac{6}{N} \sum_{i=1}^N \left( 1 - \frac{y}{H} \right) \frac{y}{H} = \frac{6}{N^2} \sum_{i=1}^N \left[ \left( i - \frac{1}{2} \right) - \frac{1}{N} \left( i - \frac{1}{2} \right)^2 \right] \quad (34)$$

Eq. (34) can be evaluated for a given  $N$ . For  $N=1, 2, 3, 4$  and  $5$ , it yields the values 1.5, 1.125, 1.05556, 1.03125 and 1.02, respectively. These numbers actually represent the velocity correction factor  $f_{corr}$ , i.e., the ratio between the (uncorrected) average particle velocity and the average velocity of the parabolic profile. Clearly,  $f_{corr}$  approaches 1 for large  $N$ 's: at higher resolution, the flow rate represented by the particles converges with the integral of the parabolic profile. Moreover, the number of particle layers does not have to be a natural number since the fluid particles can also fill a given clearance distance via a disordered arrangement. Thus, a continuous function to fit the discrete summation Eq. (34) was required. We established that the following function reproduces the values of Eq. (34) exactly:

$$f_{corr} = 1 + \frac{1}{2} \left( \frac{1}{N} \right)^2 = 1 + \frac{1}{2} \left( \frac{\Delta x}{r_1 + r_2} \right)^2 \quad (35)$$

Substituting Eqs. (19)–(21) in (24) and (25), Eqs. (24)–(26) in (27) and (28) and Eqs. (27) and (28) in Eq. (30) yields the following momentum equation in the clearance:

$$\frac{d\vec{v}_a}{dt} = - \frac{\sum_b m_b \left( \frac{p_a}{\rho_a^2} + \frac{p_b}{\rho_b^2} + R(f_{ab})^4 \right) \vec{\nabla}_a W_{ab}}{\sum_b \frac{m_b}{\rho_b} W_{ab}} + \frac{2\eta_a}{r_2 \rho_a} \left( \frac{\vec{v}_{w,2} - \vec{v}_{w,1}}{r_1 + r_2} - \frac{\vec{v}_a - \vec{v}_{w,1}}{r_1} \right) \cdot f_{corr} + \vec{a} \quad (36)$$

The criteria below were established in order to substitute the SPH momentum equation Eq. (5) with the clearance model Eq. (36):

- the considered particle is in contact with two walls (the barrel and screw walls). This model was not applied to the clearance between the screws where the walls are non-parallel and the flow is more complex than assumed for the derivation of the model. However, the volume fraction of the fluid inside the clearance between the screws is much lower than that between the screws and the barrel.
- the sum of the wall distances  $r_1 + r_2$  is smaller than a pre-defined clearance distance parameter (to avoid using the clearance model in resolved regions with two adjacent walls).

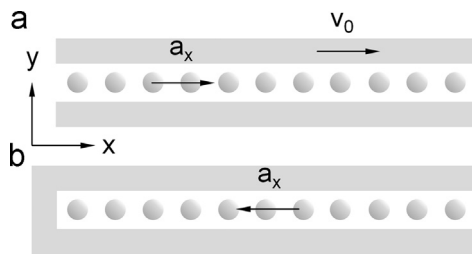


**Fig. 6.** Setup for the test cases with one layer of fluid particles across the clearance, (a) with open periodic boundaries in the  $x$ -direction and (b) one closed boundary in the  $x$ -direction. The extension in the  $z$ -direction was 5 layers of fluid particles, also with open periodic boundaries.

**Table 1**

Values of smoothing length  $h$ , initial particle spacing  $\Delta x$  and the resulting number of particle layers across the 0.5 mm clearance.

$h$ [mm]	0.6	0.3	0.2	0.12
$\Delta x$ [mm]	0.5	0.25	0.167	0.1
# Particle layers	1	2	3	5

#### 4.3.2. Validation of the clearance model

The newly developed clearance model (Eq. (36)) was incorporated in the open-source software LIGGGHTS and various tests based on a setup of an unresolved clearance flow between two parallel walls with open periodic boundaries in the remaining directions (Fig. 6a) were conducted. We studied a Couette flow, a Poiseuille flow and a superposition of both. A pressure gradient along the clearance was not applied, since the pressure on the corresponding periodic boundaries must be equal. As such, we used a body force  $a_x$  in the  $x$ -direction to achieve the Poiseuille flow.

First, we considered the Couette flow using the setup shown in Fig. 6a, i.e., a pure drag flow between two walls forming a 0.5 mm-wide clearance with a relative wall velocity of  $v_0 = 0.1$  m/s. The density was  $1000 \text{ kg/m}^3$  and the viscosity was  $1 \text{ Pas}$ , yielding a Reynolds number of 0.05. The smoothing length varied: we started at  $h = 0.6 \text{ mm}$  and refined it to  $h = 0.3 \text{ mm}$ ,  $h = 0.2 \text{ mm}$  and  $h = 0.12 \text{ mm}$ . In each case, the initial particle spacing was  $\Delta x = h/1.2$ . This yielded 1, 2, 3 and 5 layers of fluid particles per clearance distance, respectively (see Table 1). We simulated the unsteady Couette flow, beginning with a stationary fluid at  $t = 0$ . The resulting particle velocities after 0.02 ms and 0.2 ms (which was the steady state) are specified in Fig. 7, left column (the shown particle velocities were equal for all particles in the clearance due to the periodicity). The data were then compared with the exact velocity profiles (unsteady and steady) calculated from a series solution (Pozorski and Wawrenczuk, 2002):

$$v(y, t) = v_0 \cdot \sum_{n=0}^{\infty} [\text{erfc}(2 \cdot n \cdot \eta_h + \eta) + \text{erfc}(2 \cdot (n+1) \cdot \eta_h - \eta)] \quad (37)$$

$$\text{with } \eta = \frac{y}{2\sqrt{\nu \cdot t}} \text{ and } \eta_h = \frac{H}{2\sqrt{\nu \cdot t}}$$

The resulting average velocities in the clearance for the unsteady and steady states after 0.02 ms are shown in Table 2 together with the corresponding relative error compared to the series solution (Eq. (37)). Since the model is based on the steady state analytical solution, the relative errors vanished in the steady state. In the unsteady state, the relative errors were below 3% for the Couette flow.

Subsequently, to demonstrate the advantages of the new clearance model, we compared our data to the velocities predicted by the SPH method without the clearance model. In the case of one particle layer per clearance distance (Fig. 7a), due to the linear

velocity profile, the steady state velocities for both the clearance model and SPH yielded exactly the average velocity of the profile. However, after 0.02 ms the unsteady velocities varied significantly: the clearance model velocity was close to the average velocity of the exact profile (i.e., the flow rates agreed), but SPH yielded a significantly lower velocity. The situation was similar for two, three and five particle layers per clearance distance (Fig. 7d, g and j): the steady state velocities always yielded the exact values for both the clearance model and SPH, while the unsteady profiles varied. However, with the increasing resolution refinement, the SPH velocities became more accurate (nearly exact for 5 particle layers, Fig. 7j), while the clearance model velocities did not exactly match the series solution (which was not required, since the model was intended for the unresolved case).

Fig. 8a shows the flow rate over time for all Couette flow cases. Clearly, the flow rate of SPH converged with the series solution for increasing resolution refinement, while it deviated significantly for the unresolved case with one layer of particles. In contrast, the flow rate in the clearance model was close to the series solution, regardless of the resolution. Clearly, for the unresolved Couette flow, the clearance model significantly improved the flow rate prediction, compared to SPH in the unsteady case.

For the second case (the Poiseuille flow), all parameters were identical to the Couette flow, except for the body force  $a_x = 1000 \text{ m/s}^2$ . As before, we varied the resolution yielding one, two, three and five particle layers across the clearance. The resulting particle velocities are shown in Fig. 7 (middle column) in comparison with the clearance model, SPH and the following series solution (Morris et al., 1997):

$$v(y, t) = \frac{a_x}{2\nu} \cdot y(y-H) + \sum_{n=0}^{\infty} \frac{4a_x \cdot H^2}{\nu \pi^3 \cdot (2n+1)^3} \cdot \sin\left(\frac{\pi \cdot y}{H} \cdot (2n+1)\right) \cdot \exp\left(-\frac{(2n+1)^2 \cdot \pi^2 \nu \cdot t}{H^2}\right) \quad (38)$$

Numerical values for the obtained average velocities in the clearance and the corresponding relative errors are provided in Table 2. While they were in exact agreement for the steady state, errors of up to 11% occurred in the unsteady state after 0.02 ms. In contrast to the Couette flow, the velocity profile was nonlinear and the steady state results for the clearance model and SPH did not match. In case of one particle layer in the clearance, the steady state SPH velocity was more than 5-fold that of the exact average velocity due to the lack of resolution, while the corresponding clearance model velocity was in agreement with the average velocity in the exact solution. The unsteady velocity after 0.02 ms was well approximated by the clearance model, but significantly overpredicted by SPH. Similarly to the Couette results, for the steady state both the clearance model and SPH results converged with the exact profile with the increasing resolution refinement. For the unsteady profile, in contrast to the clearance model results, the SPH results converged with the exact profile. The flow rate over time for the Poiseuille flow is shown in Fig. 8b. For all of the investigated resolutions, the flow rate of the clearance model was close to the exact solution, while the SPH flow rate strongly deviated due to coarser resolution and was close to the exact value for 5 particle layers per clearance distance.

Finally, we superposed the Couette flow over the Poiseuille flow using a wall velocity of 0.1 m/s and a body force of  $-1000 \text{ m/s}^2$  (i.e., acting against the wall velocity). The other parameters were the same as above. The resulting velocity profiles and the flow rate over time are shown in Fig. 7, right column, and Fig. 8c, respectively. For the exact solution, we superposed the series solutions Eqs. (37) and (38). For 1 particle layer across the clearance, due to the strong deviation of the pressure-driven flow component, the SPH method even yielded a negative flow rate compared to the clearance model.



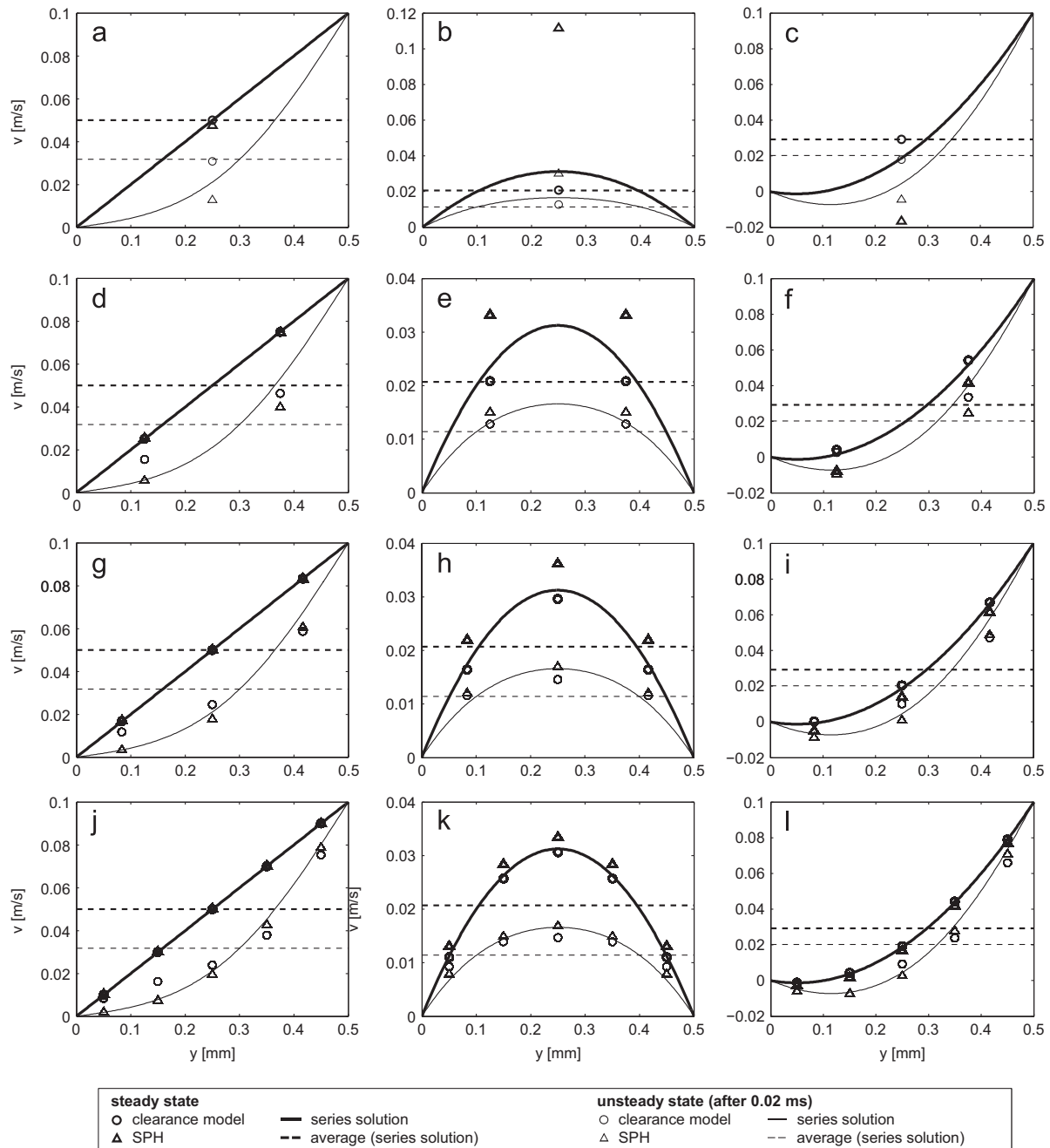


**Fig. 7.** Velocity profiles in the clearance for the Couette flow (left column), the Poiseuille flow (middle column) and the superposition of the Couette and Poiseuille flows (right column) for different numbers of particle layers in the clearance (resolution): (a–c) for 1 layer, (d–f) for 2 layers, (g–i) for 3 layers and (j–l) for 5 layers.

Since the above results did not address pressure forces, we studied the effect of body force  $a_x$  on the hydrostatic pressure in an unresolved clearance using the proposed clearance model (Eq. (36)). To that end, we used a similar setup as before, but closed the clearance at one end in the  $x$ -direction (Fig. 6b). We varied the resolution and applied the same values for the smoothing length and initial particle spacing as above (see Table 1). The body force was  $a_x = 10 \text{ m/s}^2$ , the density  $1000 \text{ kg/m}^3$  and the viscosity  $1 \text{ Pas}$ . Fig. 9 shows the resulting pressure of the fluid particles in the  $x$ -direction for the case involving one layer of fluid particles across the clearance (symbols). We fitted a linear function using these data (solid line in Fig. 9) and listed the obtained pressure gradients  $dp/dx$  in Table 3. The obtained results were close to the theoretical value of  $10,000 \text{ Pa/m}$  for all investigated cases,

and the corresponding relative errors were below 1%, indicating that the proposed normalization factor for the pressure forces in Eq. (36) was correct.

#### 4.4. Simulation parameters

In the FVM simulation reported by Bierdel (2008) the density was  $\rho = 1000 \text{ kg/m}^3$ , the viscosity was  $\eta = 1000 \text{ Pas}$  and the screw speed was  $n = 95 \text{ rpm}$ , which yielded a Reynolds number of  $Re = 0.0059$  (using the definition  $Re = nD^2\rho/\eta$ ). Since the dimensionless parameters did not depend on viscosity and screw speed, their values did not have to be matched. A decrease in viscosity was essential for the time step and computational expense. Eq. (14) suggests that an upper limitation of the time step is inversely

**Table 2**  
Average velocity and corresponding relative errors for the investigated cases.

# Of particle layers	1	2	3	5
<b>Couette flow</b>				
$v_{av}$ [m/s] (0.02 ms)	0.0308	0.0308	0.0316	0.0323
Rel. error (0.02 ms) (%)	2.8	2.8	0.3	1.9
$v_{av}$ [m/s] (steady state)	0.05	0.05	0.05	0.05
Rel. error (steady state) (%)	0.0	0.0	0.0	0.0
<b>Poiseuille flow</b>				
$v_{av}$ [m/s] (0.02 ms)	0.0128	0.0128	0.0126	0.0122
Rel. error (0.02 ms) (%)	11.3	11.3	9.6	6.1
$v_{av}$ [m/s] (steady state)	0.0208	0.0208	0.0208	0.0208
Rel. error (steady state) (%)	0.0	0.0	0.0	0.0
<b>Superposition</b>				
$v_{av}$ [m/s] (0.02 ms)	0.0180	0.0180	0.0191	0.0201
Rel. error (0.02 ms) (%)	10.1	10.1	5.4	0.5
$v_{av}$ [m/s] (steady state)	0.0292	0.0292	0.0292	0.0292
Rel. error (steady state) (%)	0.0	0.0	0.0	0.0

proportional to the viscosity ( $\Delta t < 0.125 h^2/\nu$ ). For the required number of time steps per screw revolution at high viscosities this means that:

$$(n\Delta t)^{-1} \sim \frac{\nu}{nh^2} = \frac{\eta}{nh^2\rho} = \left(\frac{D}{h}\right)^2 \frac{\eta}{nD^2\rho} = \left(\frac{D}{h}\right)^2 Re^{-1} \quad (39)$$

Eq. (39) shows that the number of time steps per screw revolution clearly depends on the smoothing length to diameter ratio  $h/D$  (i.e., the resolution) and is inversely proportional to the Reynolds number  $Re$ , which is a drawback when simulating high-viscous flows, as typical in extrusion. Optimization by choosing the involved parameters (screw speed, viscosity and length scale) is not possible. With the used method, the only way to reduce the computational expense is to increase the Reynolds number as much as possible.

Information on the creeping flow regime for twin-screw extruders is limited. Pawłowski (1971) showed experimentally that for a single-screw extruder the pressure characteristic was independent from the Reynolds number up to  $Re=40$ . We correctly assumed (see results below) that the limiting Reynolds number was similar for a twin-screw extruder and used the parameters that yielded a Reynolds number of  $Re=3.72$ , which was one order of magnitude lower than the above value ( $Re=40$ ) and was expected to fulfill the conditions for the creeping flow regime. The screw speed and viscosity were  $n=60$  rpm and  $\eta=1$  Pas, and density was kept at the original value of  $1000 \text{ kg/m}^3$  (i.e.,  $\rho_0=1000 \text{ kg/m}^3$  in Eq. (10)). Using these parameters, we simulated eight cases with a completely filled screw element (geometry A) and varied the axial pressure drop  $dp/dz=0, 5, 10, 15, 20, 25, 30$  and  $35 \text{ kPa/m}$  (Scenario 1 in Table 4). Similar as shown for the reference results (Bierdel, 2008), we applied periodic boundaries in the axial direction. Although, inflow and outflow boundaries are possible with SPH (Kruisbrink et al., 2011; Mahmood et al., 2011), periodic boundaries were more efficient in this case due to the periodicity of the geometry. Since the pressure must be equal at both periodic boundaries (i.e., zero pressure drop), we replaced the axial pressure drop  $dp/dz$  with the body force  $a_z=dp/dz/\rho$ , acting against the pumping and conveying direction ( $a_z=0, 5, 10, 15, 20, 25, 30$  and  $35 \text{ m/s}^2$ ). This superposed the pressure drop caused by the screw rotation with a hydrostatic pressure gradient, yielding a zero pressure drop together.

As discussed above, the spacing we chose was fine enough to allow the flow of fluid particles through the tightest clearances of the geometry with only one layer of fluid particles. In co-rotating twin-screws, the tightest clearance distance is typically between the screws and the barrel (depending on the method of creating

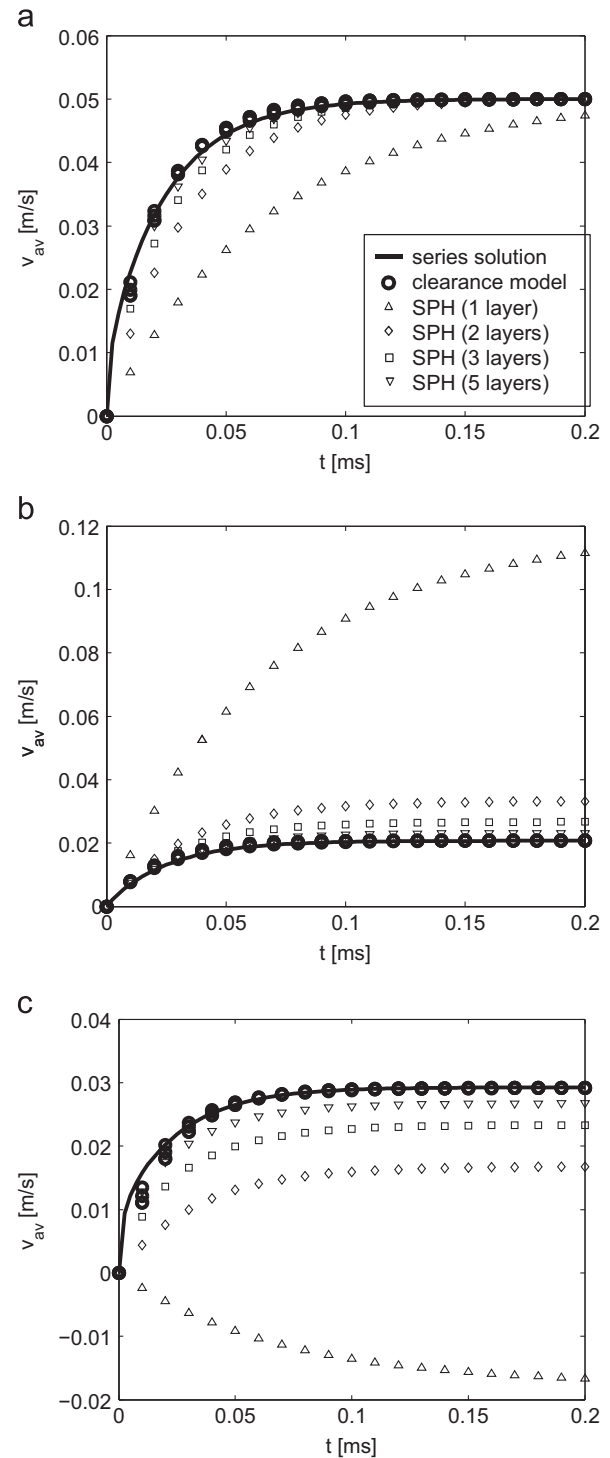


**Fig. 8.** Flow-rate-equivalent average velocity  $v_{av}$  over time  $t$  for the (a) Couette flow, (b) Poiseuille flow and (c) superposition of the Couette and Poiseuille flows. The data for SPH are shown for various resolutions, yielding one, two, three and five layers of particles across the clearance. In the clearance model, these 4 lines almost overlapped.

the clearances, the tightest clearance may be between the screws, specifically for small pitches). In our case, since this distance was  $0.5 \text{ mm}$ , we set the initial particle spacing  $\Delta x$  to  $0.5 \text{ mm}$  and the smoothing length to  $1.2$  times of  $\Delta x$  ( $h=0.6 \text{ mm}$ ). The initial particle positions were at the nodes of a cubic lattice, with a distance of at least  $\Delta x/2$  between the particle centers and the walls, since particles closer to the wall surface can blow up the simulation due to the wall repulsion (Eq. (16)). This resulted in

981,278 fluid particles for the completely filled cases. The mass of the fluid particles was determined as the entire mass of the fluid (calculated from the geometry's free volume of 132,617 mm<sup>3</sup>) divided by the number of the particles.

The particle initialization in a complex geometry is not trivial, since in general a regular initial arrangement of the particles does not exactly match the shape of the boundaries, which causes empty spaces between fluid and boundaries. This could be avoided by a recently proposed particle packing algorithm, which achieves a particle initialization that matches the shape of the geometry well (Colagrossi et al., 2012). Moreover, this strongly reduces the numerical noise caused by the particle rearrangement in the early stages of the simulation. However, in our work it was sufficient to initialize the particles on a regular lattice. In order to compensate the resulting empty spaces between fluid and boundaries, we set the initial density of the particles higher than the desired 1000 kg/m<sup>3</sup>, which caused a slight expansion of the weakly compressible fluid during the first time steps, sufficient to fill the entire volume. However, it was difficult to determine the initial density that would yield the average density of the fluid particles after expanding to be 1000 kg/m<sup>3</sup>. Although the exact

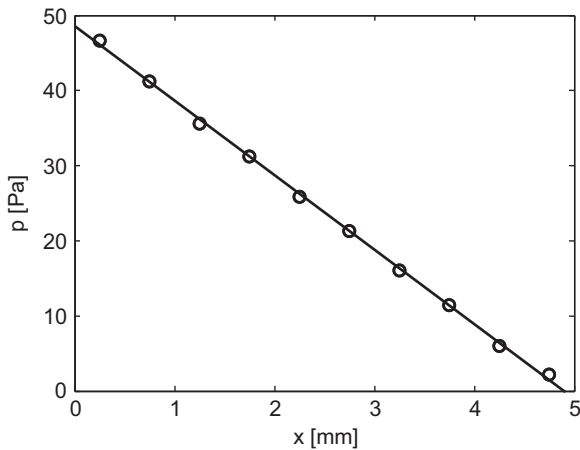


**Fig. 9.** Hydrostatic pressure profile in a 0.5 mm wide clearance with one layer of fluid particles (symbols indicate the pressure of the fluid particles, the linear function is a fit).

**Table 3**  
Obtained hydrostatic pressure gradient and corresponding relative error for the investigated cases.

# Of particle layers	1	2	3	5
$dp/dx$ [Pa/m]	9911	10079	9988	10032
Relative error (%)	0.89	0.79	0.12	0.32

**Table 4**  
Simulation parameters.

Scenario	Geometry	$n$	$\eta$	$Re$	$h$	$c$	$p_0$	$C_{rep}$	$\rho_{init}$	$\Delta t$	$(n\Delta t)^{-1}$
		[rpm]	[Pas]	–	[mm]	[m/s]	[Pa]	[mN]	[kg/m <sup>3</sup> ]	[μs]	[10 <sup>3</sup> ]
1, 2	A	60	1	3.72	0.6	15	500	2–3	1050	5	200
3	B	60	1	3.72	0.6	15	500	2–3	1050	5	200
4	A	60	2	1.86	0.6	15	500	3	1050	5	200
5	A	60	0.2	18.6	0.6	15	100	0.5	1050	10	100
6	A	150	1	9.30	0.6	15	500	2	1050	5	80
7	A	60	1	3.72	1.2	15	500	10	1120	5	200
8	A	60	1	3.72	0.6	7.5	0	25–100	1081	1–5	200–1000
9	C	60	1	3.72	0.6	15	500	3	1080	5	200

value of the density is unimportant for creeping flows, the equation of state for a weakly compressible fluid (Eq. (10)) shows that pressure strongly depends on small density variations. Thus, pressure values could easily be negative, causing formation of partially filled regions, or too high, enhancing the time step limitation due to higher interaction forces. We iteratively established that an initial density of  $\rho_{init}=1050$  kg/m<sup>3</sup> was appropriate in this case and the resulting average density of the fluid was slightly above 1000 kg/m<sup>3</sup> (within a range of 0.5%).

Moreover, we used a background pressure  $p_0 > 0$  in the equation of state. Otherwise, the pressure values would be distributed around zero for the density distributed around  $\rho_0=1000$  kg/m<sup>3</sup>, resulting in the formation of partially filled regions at negative pressure. A value of  $p_0=500$  Pa was sufficient to keep the screw element completely filled.

For the speed of sound, we used the values recommended in Eq. (11). The maximum fluid velocity was estimated by the circumferential screw velocity  $v_0=D_o\pi n=0.188$  m/s (for 60 rpm). With  $\delta=0.01$  (i.e., allowing approximately 1% density variation in the flow field), the first criterion of Eq. (11) yielded  $c > 1.88$  m/s. For the length scale  $L_0$  of the second criterion, the clearance distance ( $L_0=0.5$  mm) was used since the highest shear rates and highest viscous forces were expected in the clearances. This yielded  $c > 6.13$  m/s. To calculate the third criterion, we used the length of the screw element ( $L_0=60$  mm) since the axial body force acted over this length, yielding  $c > 14.49$  m/s. In the end, we set the speed of sound to  $c=15$  m/s, the limiting criterion being the (maximum) applied body force of 35 m/s<sup>2</sup>.

Based on this, we calculated the required time step as shown in Eqs. (14) and (15). The CFL criterion in Eq. (14) yielded  $\Delta t < 10$  μs, the second criterion yielded  $\Delta t < 45$  μs due to the viscosity and the third criterion yielded  $\Delta t < 1035$  μs due to the body force. Clearly, the body force did not limit the time step in this case. Eq. (15), which involves both, the CFL and viscosity criteria, yielded  $\Delta t < 5.14$  μs (with  $\alpha=10\nu/hc=1.11$ ). Since, according to Eq. (15), the effect of the viscosity was still present ( $1.2\alpha$  is in the same order of magnitude as 1), we used a time step of  $\Delta t=5$  μs, requiring a number of  $2 \times 10^5$  steps per screw revolution at 60 rpm. A time step of 10 μs was not sufficient and led to unstable simulations.

While investigating the required time step, we established that stability strongly depended on the applied wall repulsion (Eq. (16)). As mentioned above, the exponents  $\alpha=1$ ,  $\beta=0$  were beneficial, and the value of the parameter  $C_{rep}$  was crucial for stability. In order to rationally determine the value of  $C_{rep}$ , we considered the underlying interaction forces that have to be balanced by wall repulsion to avoid wall penetration. The viscous forces are irrelevant, since they act tangentially on the walls. In contrast, the pressure forces act perpendicularly to the walls, but are mainly balanced by the pressure term of the applied wall interaction. We established that increasing the pressure level (i.e.,

increasing background pressure  $p_0$ ) required a higher repulsion parameter  $C_{rep}$  for stability. To that end, we estimated  $C_{rep}$  based on the comparison of wall repulsion and pressure forces due to the actual pressure  $p$ :

$$C_{rep} \sim \frac{m^2 p}{\rho^2 h^4} \quad (40)$$

The right hand side was derived from the momentum equation (Eq. (5)), where the pressure term was proportional to  $mp/\rho^2$ , the kernel gradient scaled with  $h^{-4}$  and the particle mass  $m$  was multiplied to convert acceleration into the force. Since the particle mass  $m$  may be expressed as density  $\rho$  times volume and the particle volume is proportional to  $h^3$ , Eq. (40) can be simplified to  $C_{rep} \sim h^2 p$ . Our simulations confirmed that the following estimation yielded useful values for  $C_{rep}$ :

$$C_{rep} \approx 10h^2 p \quad (41)$$

where  $p$  is an average value of the expected pressure distribution (e.g.,  $p_0$ , if the density is distributed around  $\rho_0$ ).

From Eq. (41) we estimated the value of  $C_{rep}$  for the completely filled cases based on the background pressure  $p_0$ . Since the density was slightly above  $1000 \text{ kg/m}^3$  and, consequently, the obtained average pressure was higher than  $p_0$ , the chosen values for  $C_{rep}$  (shown in Table 4) were approximately 50% higher than recommended by Eq. (41). Nevertheless, the exact value of  $C_{rep}$  was less critical, rather the order of magnitude.

In order to investigate the extent to which our new clearance model improved the quantitative agreement, we repeated three cases of Scenario 1 without it (denoted as Scenario 2), while using all other parameters as in Scenario 1. To demonstrate the effect of the clearances on the results, we repeated three simulations with geometry B (Fig. 1), with the clearances between the screws and barrel completely closed (Scenario 3).

To show that the above modifications to viscosity and the screw speed had a vanishing effect on the results, we repeated one simulation according to Scenario 1 with varied viscosity (Scenario 4 with 2 Pas and Scenario 5 with 0.2 Pas) and a varied screw speed (Scenario 6 with 150 rpm). The corresponding changes to other parameters are stated in Table 4.

Furthermore, we repeated four simulations of Scenario 1 with a lower resolution (Scenario 7 with  $\Delta x = 1 \text{ mm}$ ,  $h = 1.2 \text{ mm}$ ) and less computational expense (112,148 particles) at the cost of the clearance flow, since the fluid particles were too large to pass through the clearances.

Scenario 8 involved simulations of the partially filled screw element (geometry A), where most parameters were the same as in Scenario 1. The body force was set to zero, since a partially filled element does not convey against pressure. Instead of that, we varied the filling ratio. For the initial particle positions, we separated the element into a completely filled section and an empty section according to the filling ratio in the axial direction, which was the simplest way to determine the filling ratio exactly. After the first screw revolution, the fluid was uniformly distributed in the axial direction, which is typical for partially filled conveying elements. The background pressure was set to zero. Although the initial expansion of the fluid was not required for the partially filled element, we applied it to achieve the same number of particles per volume as in the completely filled simulations. In contrast, the initial density  $\rho_{init}$  was determined differently: in the partially filled case, where no compression of the fluid was possible, the expansion always achieved the average pressure of zero and the average density of  $1000 \text{ kg/m}^3$ , regardless of the applied value of  $\rho_{init}$ . Thus, we calculated the initial density for the partially filled simulations based on the particle mass and the initial particle spacing, which yielded  $\rho_{init} = 1081 \text{ kg/m}^3$ .

Furthermore, since stability problems intensified with the decreasing filling ratio in the partially filled simulations, we changed the value of the speed of sound. We reduced  $c$  to  $7.5 \text{ m/s}$  in the partially filled element, which was reasonable in the absence of the body force. Using that, we simulated the filling ratios of 1, 0.95, 0.9, 0.75 and 0.5. For lower filling ratios, we additionally had to decrease the time step to avoid stability problems ( $2.5 \mu\text{s}$  for filling ratios 0.25 and 0.1, and  $1 \mu\text{s}$  for filling ratio 0.05).

Eq. (41) was not suitable for determining the wall repulsion parameter  $C_{rep}$  for the partially filled element, where the fluid was not as compressed as in the completely filled state. Interestingly, we found that the required values of  $C_{rep}$  in the partially filled state were significantly larger than those in the completely filled state ( $C_{rep}$  was iteratively determined, see Table 4 for the obtained values). The reason for that, as well as for the increased stability problems at low filling ratios, is currently unclear, and more detailed investigations are required.

Finally, we repeated two simulations with Scenario 1 with geometry C (Fig. 1) after we learned that our method for creating geometry A was different from the one described in (Bierdel, 2008). This led to Scenario 9, under which we calculated only 1 revolution to yield pressure drop and power to compare the results with (Bierdel, 2008). These simulations are not included in the mixing studies described below.

## 5. Results and discussion

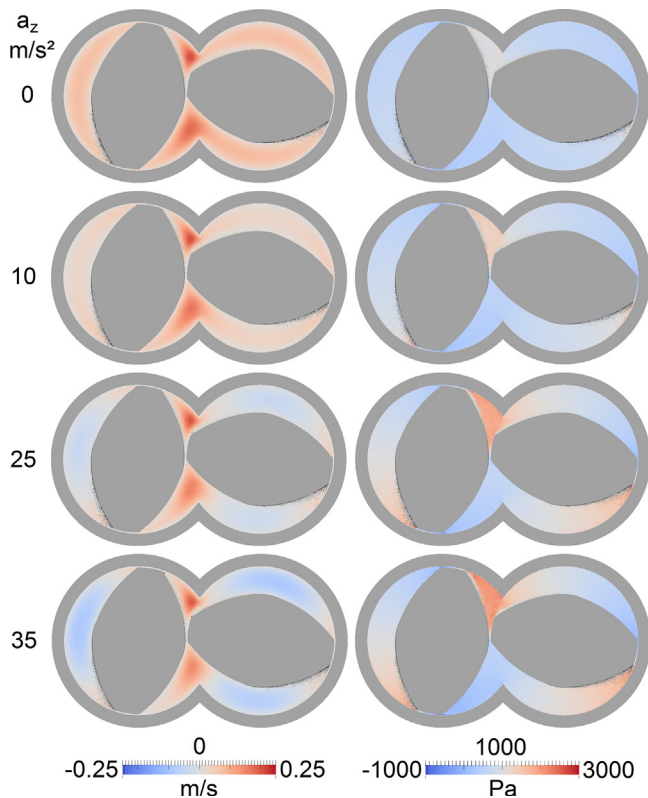
The simulations were performed at 32 Intel XEON cores (2.0 GHz) and 128 GB RAM. The required computation time for one screw revolution ( $2 \times 10^5$  time steps) and  $10^6$  particles was about 40 h. This might be more than required for mesh-based CFD methods, which can save a lot by varying the spatial resolution. However, if also mixing should be investigated using tracer particles – see Part 2 of this work – a high particle number is required also for CFD which eliminates this drawback.

Fig. 10 illustrates the axial velocity and the pressure distribution over the cross-section of the completely filled screw element for variable backpressure (snapshots from simulations under Scenario 1). The angular position of the screws was chosen arbitrarily ( $9^\circ$  off the vertical direction). The rotation was in the clockwise direction and the conveying direction was towards the observer.

Case  $a_z = 0 \text{ m/s}^2$  (top) showed only positive axial velocity values, clearly, the rotating screws conveyed all the material in the same direction (except negligible negative values in the clearances between screws and barrel, where the pressure caused a slight backflow). This case represents inherent conveying, i.e., the resulting dimensionless flow rate is the  $A_1$ -parameter in Eq. (1). The highest axial velocity occurred in the nip region, where the screws intermeshed. In the screw channels, far from the nip region, the axial velocity was lower (ca. 40% of the maximum) and reached zero at the wall surfaces due to the no-slip condition. However, the peak values of the axial velocity did not dominate the flow rate since the region where the peak values occurred was only a small fraction of the entire cross section area. The corresponding pressure profile showed the maximum values at the top of the nip region, where the fluid was compressed in a chamber of the geometry, and the minimum values in the back of the screw flights.

With the increasing backpressure (i.e., increasing  $a_z$ ), the velocity maxima in the nip region remained similar due to the strong enforcement of the flow by the movement of the geometry in this region. However, in the screw channels, the axial velocity decreased with the increasing backpressure and reached negative values at 25 and  $30 \text{ m/s}^2$ , which represented a flow through the screw channels against the conveying direction driven by





**Fig. 10.** Snapshots of the axial velocity (left column) and pressure (right column) in the cross-section of the completely filled screw element (clockwise rotation) for variable axial body force  $a_z$ .

backpressure. Clearly, the flow rate (i.e., the integral of the axial velocity over the cross section area) decreased with the increasing backpressure and became negative between 20 and 25 m/s<sup>2</sup>. The corresponding pressure profiles looked qualitatively similar to the case of 0 m/s<sup>2</sup>, but showed increasing pressure variations in the cross-section as the backpressure increased.

Similar axial velocity profiles of the half-filled screw element (Scenario 8) at 6 snapshots during  $\frac{1}{4}$  a revolution are shown in Fig. 11 (representative for other filling ratios). The pressure distribution in the partially filled state is not shown, since it was similar to the completely filled state without backpressure. These snapshots were taken from the backside to clearly show the partial filling, thus the rotation is counter-clockwise here and the conveying direction away from the observer. Fig. 12 shows a 3D view of the half-filled screw element (clockwise rotation). Specifically, the top view of Fig. 12 shows all particles, whereas in the bottom view the particles adhering to the barrel wall (i.e., with a velocity magnitude of almost zero) are suppressed in order to provide a better visibility of the free surfaces.

Figs. 11 and 12 demonstrate how the melt is distributed over the cross-section in the partially filled two-flighted conveying element, i.e., located in three regions that are forced along the barrel wall by the screws (like a snow plow clearing the road). The patterns observed in the empty regions were produced by fluid particles adhering to the screw and barrel surfaces, resulting from the flow through the clearances (in reality, this adhering material can form a thin film on the wall surfaces, at least in surface-wetting materials). As in the completely filled screw element, the maximum values of the axial velocity occurred in the nip region, while the channel regions had lower values. Negative values did not occur, similarly to the case  $a_z=0$  m/s<sup>2</sup> of the completely filled element (except slight backflow through the clearances). The latter represents the transition between the partially and completely

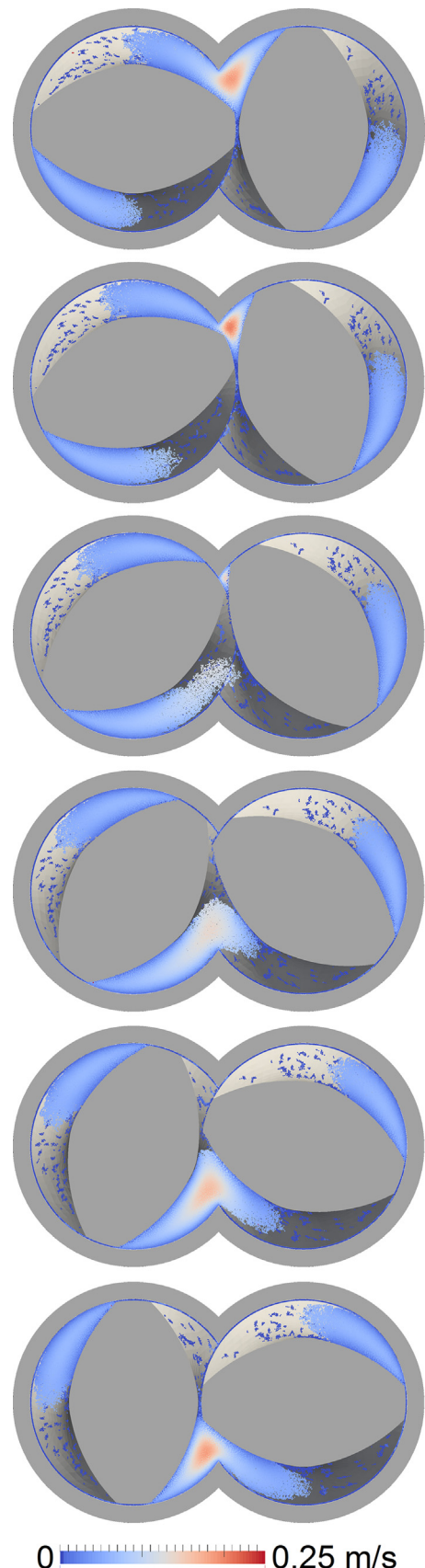


**Fig. 11.** Snapshots of the axial velocity in the cross-section of the half-filled screw element during a  $\frac{1}{4}$  revolution (counter-clockwise rotation).

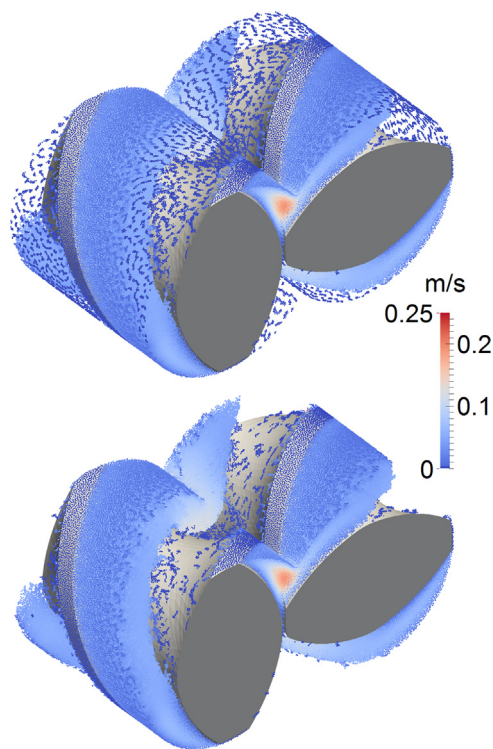


**Fig. 12.** Snapshots of the half-filled screw element and axial velocity distribution (clockwise rotation). Top: including all particles, bottom: suppressing particles at the barrel wall.

filled states, since it results from a completely filled section with backpressure approaching zero and from a partially filled section with the filling ratio approaching 1.

The representation of the free surface (mainly obvious from Fig. 11) is not fully exact, which is related to the particle discretization. Irregularities at the scale of the particle spacing occurred probably due to the continuous fluid deformation and the related particle rearrangement. This could possibly be improved by including a surface tension model.

Quantitative results for pressure, power and axial force characteristic (see Eqs. (1)–(3)) are shown in Figs. 13–15. The rotation torque and the axial force were computed from the interaction forces of each fluid particle with the STL meshes of the screws. Fig. 13 shows the pressure characteristic results for all scenarios, except for the partially filled simulations (Scenario 8 with zero backpressure), compared to the FVM result of (Bierdel, 2008). All of the results are in good agreement and show the typical pressure characteristic of a completely filled conveying element, i.e., the inherent conveying capacity at the intercept with the abscissa and a decreasing flow rate with the increasing backpressure due to the backflow through the screw channels (as qualitatively discussed above for Fig. 10).

The region of positive flow rate and positive backpressure is termed “conveying screw” (Kohlgrüber, 2008) since the screw element actively conveys against the pressure drop. Operation states with negative backpressure and flow rates that are higher than the inherent conveying capacity are referred to as “overrun screw” since they are achieved via a pressure drop in the conveying direction, which supports the flow. This region is only relevant for screw elements with a comparably low inherent conveying capacity and not for a conveying element with a pitch as large as the one we investigated. However, the region of negative flow rates, or the “backward pumping screw,” is of practical relevance, since it represents a backward-conveying element (occasionally

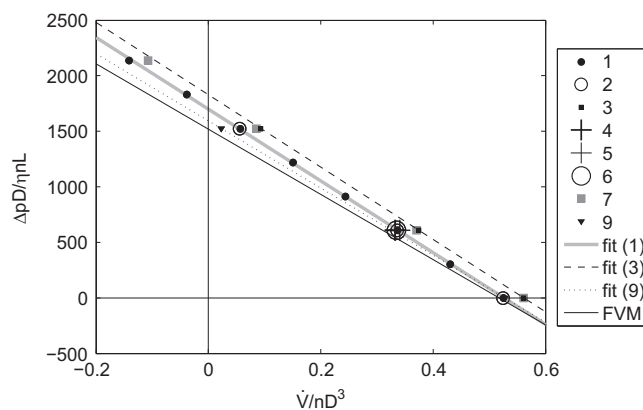


**Fig. 13.** Pressure characteristic for the completely filled simulations (Scenarios 1–7 and 9) and linear fits for Scenarios 1, 3 and 9 compared with FVM data (Bierdel, 2008).

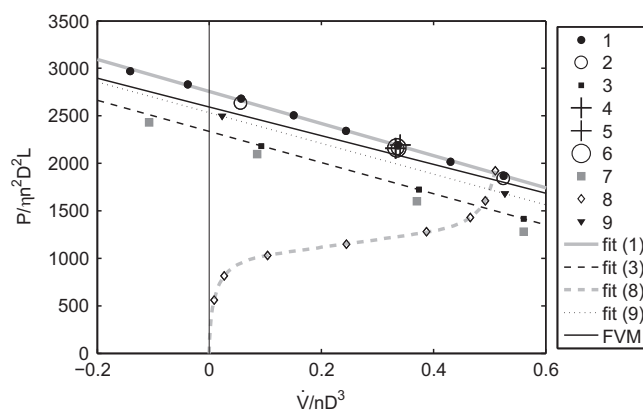


**Fig. 14.** Power characteristic in the completely filled simulations (Scenarios 1–7 and 9) together with linear fits for Scenarios 1, 3 and 9 in comparison with FVM data (Bierdel, 2008). Data points for Scenario 8 and the nonlinear fit represent the partially filled simulations.

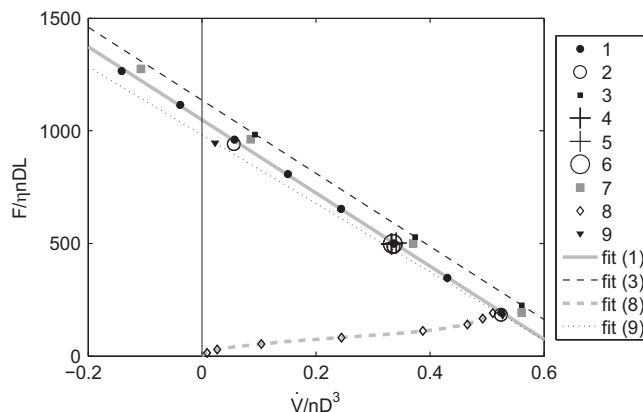


**Fig. 15.** Axial force characteristic for the completely filled simulations (Scenarios 1–7 and 9) and linear fits for Scenarios 1, 3 and 9. Data points for Scenario 8 and the nonlinear fit represent the partially filled simulations.

termed “left-handed”). Backward-conveying elements have the same shape as the corresponding forward-conveying elements but the inverted torsion. Due to the symmetry, a physically identical situation can be established by using the geometry of the forward conveying element and inverting the flow rate. As such, we yielded backward-conveying conditions with the geometry of

the forward-conveying element by increasing the backpressure sufficiently to achieve a negative flow rate.

Scenarios 1, 2, and 4–6 yielded the equivalent pressure characteristic, and Scenarios 3 and 7 deviated significantly. This is reasonable, since under Scenario 3 (geometry B with closed clearances) no backflow through the clearances occurred and, consequently, the achieved flow rate was higher than for geometry A. Although Scenario 7 also involved geometry A, the clearance flow was not present there due to the coarser resolution (1 mm), which prevented fluid particles from passing the 0.5 mm clearances. As a result, Scenario 7 yielded a similar pressure characteristic as Scenario 3.

The coincidence of Scenarios 1 and 4–6 confirms the independence of the pressure characteristic on variations of viscosity and screw speed in the case of Newtonian, temperature-independent, creeping flow.

The similarities of Scenarios 1 (with the clearance model) and 2 (without the clearance model) show that our new clearance model has a vanishing effect on the pressure characteristic. The reason is the type of flow within the clearances between the screws and the barrel, which is the superposition of a drag flow (caused by the relative velocity) and a pressure-driven flow (caused by the pressure difference between adjacent screw channels). The clearance flow is dominated by the drag flow, which was e.g., shown in (Bierdel, 2008) and can be easily confirmed as follows: The pressure difference along the clearance in circumferential direction of about 2000 Pa (see Fig. 10) and the viscosity of 1 Pas yield an average velocity of 0.0083 m/s in a 0.5 mm tight and ca. 5 mm long clearance (based on the analytical solution for the Poiseuille flow, see e.g., Eq. (17)), whereas the circumferential velocity of 0.188 m/s at 60 rpm yields an average velocity of 0.094 m/s for the drag flow, which is about 10 times as much. As shown above, the SPH equations yield the exact velocity in unresolved clearances for the steady state in a pure Couette flow. Together with the small volume of the clearances compared to the entire volume, the global variables show vanishing errors for the considered simplified scenario of a Newtonian, temperature-independent fluid. However, in further developments, which account for the local energy dissipation rate and local temperature of the fluid, significant errors can be expected without appropriate clearance modeling.

Although the SPH simulations for Scenarios 1–7 yielded good results, they deviated somewhat from the FVM results (Bierdel, 2008), especially in terms of pressure drop at zero flow rate that was about 12% higher in our simulations for geometry A. The main reason was the above-mentioned difference in the method for creating the clearances, which yielded the same main dimensions of the screw element but smaller clearance distances in some regions between the screws and a higher pressure drop in geometry A than in geometry C. When geometry C was generated via the same clearance formation method as the one described in (Bierdel, 2008), the agreement of the pressure characteristic significantly improved (Scenario 9) and the remaining deviation of the axis intercepts  $A_1$  and  $A_2$  was below 5%. Clearly, numerical methods are never exact and the deviations may be caused by small errors of both methods.

The values of the determined parameters  $A_1$  and  $A_2$  for the fits under Scenarios 1, 3 and 9 and the FVM results (Bierdel, 2008) are shown in Table 5.

The power characteristics shown in Fig. 14 show analogous results: they were nearly identical for Scenarios 1, 2, and 4–6, but for Scenarios 3 and 7 yielded a significantly lower driving power due to the absence of clearance flow between the screws and barrel with correspondingly high power consumption. The power characteristic of geometry A (Scenario 1) has higher power values than that of geometry C (Scenario 9) due to the smaller clearance distance between the screws. The obtained  $B_1$  and  $B_2$  parameter values are shown in Table 5. The deviation between Scenario 9 and

the FVM results (Bierdel, 2008) was below 3% for the  $B_2$  parameter and almost 10% for the  $B_1$  parameter. With increasing backpressure, i.e., decreasing flow rate, the power of the completely filled element increased due to the pumping power required for conveying against a pressure gradient and the additional dissipation power of the pressure-driven backflow.

In contrast to the pressure characteristic, a power characteristic exists for the partially filled state (Scenario 8). The driving power in the partially filled state coincides with the completely filled state at the inherent conveying, where the element is completely filled and operated without pressure drop. The driving power at that point is described via parameter  $B_5$  as proposed by (Kohlgrüber et al., 2012) (see Table 5). It is the maximum of the dimensionless driving power in the partially filled state, and can be calculated from the pressure characteristic of the completely filled element according to Eq. (2) using parameters  $A_1$ ,  $B_1$  and  $B_2$  (i.e.,  $B_5 = B_2 (1 - A_1/B_1)$ ). However, a small deviation between Scenarios 1 and 8 occurred (both for  $A_1$  and  $B_5$ ) due to the reduced speed of sound (7.5 m/s vs. 15 m/s) in the partially filled simulations (Scenario 8).

Note that for the partially filled element (Scenario 8) the flow rate is directly related to the filling ratio (this correlation is shown in detail in Fig. 16). Thus, at zero flow rate, the filling ratio is zero and at the inherent conveying capacity the filling ratio is 1 (where the curves of the partially and completely filled state converge). Due to the zero filling ratio, the driving power is also zero at zero flow rate. With the increasing flow rate (and filling ratio), a nonlinear increase of the driving power was observed. The nonlinearity was especially significant above a filling ratio of 0.75 and below 0.25, which was possibly due to higher shear rates near the borders of the screw channels than in the center. Considering, for example, a half filled screw, a small increase of the filling ratio requires the additional fluid to be located in the center of the

**Table 5**  
Resulting screw parameters.

Scenario	1	3	8	9	FVM (Bierdel, 2008)
$A_1$	0.526	0.561	0.510	0.527	0.518
$A_2$	1699	1829	–	1594	1521
$B_1$	1.629	1.425	–	1.566	1.714
$B_2$	2756	2334	–	2535	2595
$B_5$	1866	1415	1921	1681	1812
$C_1$	0.645	0.700	–	0.646	–
$C_2$	1048	1135	–	980.8	–
$C_5$	193.4	225.4	191.7	179.7	–

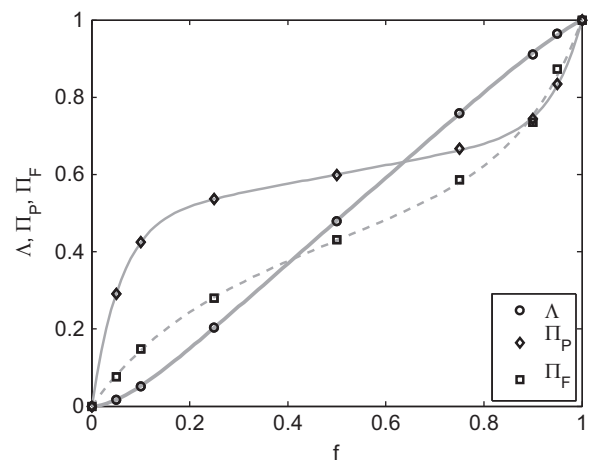


**Fig. 16.** Simulation results and fits for normalized flow rate  $\Lambda$ , power  $\Pi_p$  and axial force  $\Pi_F$  versus filling ratio  $f$ .



channels. Here, the channel depth is the largest and the shear rate is minimal, causing a relatively low increase of the driving power. In contrast, for filling ratios close to 0 or 1, the same increase of the filling ratio requires the additional fluid to be located near the borders of the channel, where the shear rate is higher than in the center due to the adjacent wall surfaces. This causes a comparably high increase of the driving power, resulting in the observed nonlinear curve. An additional reason for the strong increase of the driving power at zero flow rate is the clearance flow. Consequently, even when the screw is almost empty, the clearances between screws and barrel are filled, causing significant power consumption due to the high shear rates there.

The axial force characteristics (Fig. 15) showed similar trends. These data were not available in (Bierdel, 2008) since they are of less practical significance, and thus, no comparison to FVM data can be made. However, for the construction of the screw's axial bearings it is important to consider the axial forces. Clearly, in the completely filled element the axial force strongly depends on the backpressure, whereas in the partially filled screw element it decreases with the decreasing flow rate (and the decreasing filling ratio), similarly to the driving power. Table 5 shows the resulting parameters  $C_1$ ,  $C_2$  and  $C_5$  (the latter is analogous to  $B_5$  for the axial force characteristic and can be calculated from the axial force characteristic of the completely filled screw element according to Eq. (3) ( $C_5 = C_2 (1 - A_1/C_1)$ )).

Results for the partially filled screw element are shown in Fig. 16 in detail. We normalized the flow rate, the power and the axial force between 0 and 1 to achieve a more general representation. To that end, we used the normalized flow rate proposed by Pawlowski (Pawlowski, 1971):

$$\Lambda = \frac{\dot{V}}{\dot{V}_{f=1}} = \frac{\dot{V}}{A_1 n D^3} \quad (42)$$

where  $\dot{V}_{f=1}$  is the flow rate of the completely filled screw element operated without pressure drop (i.e., inherent conveying). Similarly, we described the normalized power  $\Pi_P$  and normalized axial force  $\Pi_F$ :

$$\Pi_P = \frac{P}{P_{f=1}} = \frac{P}{B_5 \eta n^2 D^2 L} \quad (43)$$

$$\Pi_F = \frac{F}{F_{f=1}} = \frac{F}{C_5 \eta n D L} \quad (44)$$

Although the normalized flow rate was almost equal to the filling ratio (Fig. 16), slight nonlinearities occurred at the filling ratios  $f < 0.2$  and  $f > 0.8$ . Specifically, at low filling ratios this is caused by the clearances and the associated wall films. The screws can only convey efficiently if the fluid is pushed by the (apparent) axial movement of the rotating screw flights. However, at filling ratios below 0.1 a significant amount of the fluid is distributed over the wall surfaces and thus, experiences only a poor conveying. This causes  $\Lambda < f$  at low filling ratios. Due to this nonlinear correlation between  $f$  and  $\Lambda$ , the curves for power and axial force versus filling ratio looked slightly different to the corresponding curves in Figs. 14 and 15, where the abscissa showed the flow rate. Similar curves for the flow rate and the power versus filling ratio of a partially filled conveying element were also shown by Pokriefke (2005), who used the FVM method with an Eulerian multiphase model. We applied the following mathematical functions to fit these data:

$$\Lambda = f - \alpha_0(1-f)[1 - (1-f)^{\alpha_0}] + \alpha_1 f(1-f^{\alpha_1}) \quad (45)$$

$$\Pi_P = f + \beta_0(1-f)[1 - (1-f)^{\beta_0}] - \beta_1 f(1-f^{\beta_1}) \quad (46)$$

$$\Pi_F = f + \gamma_0(1-f)[1 - (1-f)^{\gamma_0}] - \gamma_1 f(1-f^{\gamma_1}) \quad (47)$$

The values of the fitted parameters  $\alpha, \beta, \gamma, \phi, \chi, \psi$  (index 0 and 1) are given in Table 6.

In order to confirm that the resulting Reynolds number of 3.72 was in the creeping flow regime, additional simulations were performed that were identical to those of Scenarios 4 and 5 (Table 4) but with varying viscosity values down to 0.035 Pas, resulting in  $Re$  numbers as large as 106. The dimensionless flow rate versus the Reynolds number is shown in Fig. 17 (together with the corresponding simulations for Scenarios 1 and 4–6). As can be seen the flow rate was constant for  $Re \leq 10$ , but deviated significantly for  $Re > 10$ . This agrees well with experimental observations of Pawlowski (1971) who showed that at  $Re \leq 40$  the pressure characteristic of a single-screw extruder did not depend on the Reynolds number.

## 6. Summary and conclusions

In this work, we presented a new approach based on the SPH method for detailed flow simulations in complex geometries. We applied this to the simulation of a Newtonian, temperature-independent flow in a completely and partially filled conveying element of a co-rotating twin-screw extruder.

We developed a new model that accounts for the flow in unresolved clearances. The model was in exact agreement with the analytical solution for a Newtonian, developed steady-state flow and the deviations for unsteady flow were low. For the investigated conveying element, our results were in excellent agreement with the FVM results from the literature, demonstrating that our method accounts correctly for the flow field under the simplified scenario of a Newtonian, temperature-independent flow.

Several variations of parameters and geometry showed that the dimensionless results were robust with respect to viscosity, screw speed and resolution, whereas the clearance flow had significant

**Table 6**  
Fitted parameters of the partially filled screw element (for index 0 and 1).

	0	1
$\alpha$	0.0765	0.0373
$\beta$	0.480	0.280
$\gamma$	0.182	0.321
$\phi$	13	11
$\chi$	16	15
$\psi$	6	8

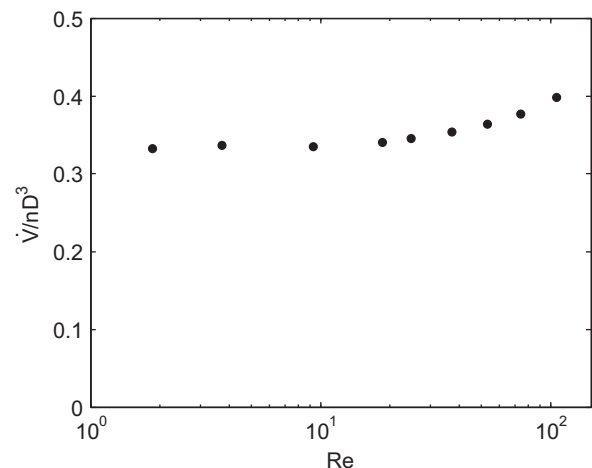


**Fig. 17.** Dimensionless flow rate versus the Reynolds number.



impact on the results. However, without considering the local energy dissipation rate and the temperature inhomogeneity, the impact of the developed clearance model was low, i.e., the results of the simulations including the clearance model were almost the same compared to the simulations without the clearance model. Nevertheless, for future investigations including the temperature field significant errors can be expected in the local dissipation rate and temperature in clearances without appropriate clearance modeling or sufficient resolution.

As stated above, we applied our method to examine the flow in a partially filled screw element, which is a major advantage of the SPH method over mesh-based CFD. This is the first study that offers a detailed analysis of the flow field in a partially filled conveying element based on SPH.

Clearly, the chosen values for viscosity (1 Pas) and pressure gradient (0–35 kPa/m) are not typical for real extrusion processes. Also, the used screw speed (60 rpm) was relatively low, specifically when considering processes in the polymer industry. As explained in detail above, the only limitation for the computational expense is the Reynolds number. Thus, there is no limitation for the screw speed as long as the Reynolds number is not changed. Using the 10-fold screw speed and the 10-fold viscosity would not require more time steps per screw revolution, i.e., the computational expense per screw revolution would be the same with 600 rpm and 10 Pas. A further increase of the viscosity (and correspondingly the pressure gradient) up to typical values in the order of 1000 Pas (factor 100) would decrease the Reynolds number and increase the number of time steps per screw revolution by the same factor. Clearly, this would lead to unacceptable computation times. It can be expected that implicit SPH schemes would be beneficial and could significantly reduce the computation costs (Cummins and Rudman, 1999; Shao and Lo, 2003; Ihmsen et al., 2014). However, it can be easily obtained from the Stokes equations that in the creeping flow regime a variation of the viscosity (or a constant prefactor for a non-Newtonian viscosity function) would not change the velocity field. Only the pressure gradients would be changed by the same factor as the viscosity. This makes the question of higher viscosities unnecessary. In contrast, the thermal energy equation would be strongly affected by a changed viscosity value, thus the use of the unchanged (real) viscosity value would be required here. At first sight, the use of two different viscosity values (functions) for the momentum and energy equations seems to be a contradiction, however, the viscosity reduction factor required for the momentum equation can be considered as an internal numerical requirement of the method, which has theoretically no effect to the solution of the momentum equation (except the pressure values, which are not coupled to the energy equation for incompressible flow).

The assumed Newtonian, isothermal flow is not the case in real extrusion processes. As this is the first study, which applied SPH for the detailed and quantitative analysis of the flow in a geometry typical for co-rotating twin-screw extruders, the focus was mainly on the complex screw geometry and the required boundary conditions. The obtained agreement of this simplified scenario with FVM data is a robust basis for further steps in this field. SPH models for non-Newtonian flow, thermal energy and viscoelasticity are existing and have to be included in future work. In this case, a generalization of the proposed clearance model would be required which could be achieved by resolving the velocity and temperature profiles across the clearance numerically, i.e., to store the cross-profiles numerically for each fluid particle inside the clearance. The Lagrangian transport of these profiles due to the actual fluid particle velocities could be calculated from the governing equations. This would still be much more efficient than refining the particle resolution in the clearances, which would yield a uniform refinement in each spatial direction.

The proposed method is a unique tool for further investigations of the flow in various types of screw elements, e.g., kneading and mixing elements. Its main advantages for co-rotating twin-screw extruders compared to mesh-based methods are: (i) SPH is mesh-free, (ii) it can easily account for free surface flows, and (iii) it facilitates the investigation of mixing by tracking tracer particles. In particular, as a Lagrangian method, SPH inherently accounts for convective mixing without numerical diffusion, as typically a drawback with mesh-based methods. A detailed analysis of the mixing phenomena is presented in Part 2 (Eitzlmayr and Khinast, 2015). Being the basis for refining empirical models of completely and partially filled screw elements, our results may lead to further improvement of more time-efficient 1D simulation tools for the study of the entire extrusion process. This can significantly facilitate design, optimization and scale-up of extrusion processes.

## Notation

### Latin symbols

$A_1, A_2$	axis intercepts of the pressure characteristic [-]
$A_{\text{contact}}$	wall contact area [m <sup>2</sup> ]
$a$	mass specific body force [m/s <sup>2</sup> ]
$B_1, B_2$	axis intercepts of the power characteristic [-]
$B_5$	dimensionless driving power at the inherent conveying [-]
$C$	centerline distance [m]
$C_1, C_2$	axis intercepts of the axial force characteristic [-]
$C_5$	dimensionless axial force at the inherent conveying [-]
$C_{\text{rep}}$	parameter for the repulsive wall force [N]
$c$	speed of sound [m/s]
$D$	barrel diameter [m]
$D_i$	inner screw diameter [m]
$D_o$	outer screw diameter [m]
$f$	filling ratio [-]
$f_{ab}$	parameter used in the tensile correction [-]
$f_{\text{corr}}$	velocity correction factor [-]
$F$	screw axial force [N]
$F_{\text{rep}}$	repulsive wall force [N]
$H$	clearance distance [m]
$h$	smoothing length [m]
$L$	length [m]
$m$	mass [kg]
$N$	number of revolutions [-]
$n$	screw speed [s <sup>-1</sup> ]
$P$	power [W]
$p$	pressure [Pa]
$p_0$	background pressure [Pa]
$\vec{r}$	particle position [m]
$r$	wall distance [m]
$r_0$	interaction length of the repulsive wall force [m]
$R$	parameter used in the tensile correction [m <sup>5</sup> /kg s <sup>2</sup> ]
$Re$	Reynolds number [-]
$\Delta t$	time step [s]
$\dot{V}$	flow rate [m <sup>3</sup> /s]
$\vec{v}$	velocity [m/s]
$W_{ab} = W( \vec{r}_{ab} , h)$	kernel function evaluated for particles $a$ and $b$ [m <sup>-3</sup> ]
$\Delta x$	particle spacing [m]

### Greek symbols

$\alpha$	artificial viscosity [-]
----------	--------------------------

$\alpha_0, \alpha_1, \beta_0, \beta_1, \gamma_0, \gamma_1$	fitted parameters [-]
$\eta$	dynamic viscosity [Pa·s]
$\Lambda$	normalized flow rate [-]
$\nu$	kinematic viscosity [m <sup>2</sup> /s]
$\Pi_F$	normalized axial force [-]
$\Pi_P$	normalized driving power [-]
$\rho$	density [kg/m <sup>3</sup> ]
$\rho_0$	reference density in the equation of state [kg/m <sup>3</sup> ]
$\tau_w$	wall shear stress [Pa]
$\phi_0, \phi_1, \chi_0, \chi_1, \psi_0, \psi_1$	fitted parameters [-]

## Acknowledgments

This work was funded through the Austrian COMET Program (grant number 834224) by the Austrian Federal Ministry of Transport, Innovation and Technology (BMVIT), the Austrian Federal Ministry of Economy, Family and Youth (BMWFI) and by the State of Styria (Styrian Funding Agency SFG). The authors would like to thank NAWI Graz for providing access to the high-performance computing system dcluster.tugraz.at. Special thanks goes to Stefan Radl (Graz University of Technology, Institute for Process and Particle Engineering) for assistance with the LIGGGHTS code and to Christoph Kloss (DCS Computing GmbH) for assistance with processing of STL meshes in LIGGGHTS.

## References

- Adami, S., Hu, X.Y., Adams, N.A., 2013. A transport-velocity formulation for smoothed particle hydrodynamics. *J. Comput. Phys.* 241, 292–307. <http://dx.doi.org/10.1016/j.jcp.2013.01.043>.
- Bahloul, W., Oddes, O., Bounor-Legaré, V., Méliis, F., Cassagnau, P., Vergnes, B., 2011. Reactive extrusion processing of polypropylene/TiO<sub>2</sub> nanocomposites by in situ synthesis of the nanofillers: experiments and modeling. *AIChE J.* 57, 2174–2184. <http://dx.doi.org/10.1002/aic>.
- Barrera, M.A., Vega, J.F., Martínez-Salazar, J., 2008. Three-dimensional modelling of flow curves in co-rotating twin-screw extruder elements. *J. Mater. Process. Technol.* 197, 221–224.
- Bertrand, F., Thibault, F., Delamare, L., Tanguy, P.A., 2003. Adaptive finite element simulations of fluid flow in twin-screw extruders. *Comput. Chem. Eng.* 27, 491–500.
- Bierdel, M., 2008. Computational fluid dynamics. In: Kohlgrüber, K. (Ed.), *Co-Rotating Twin-Screw Extruders*. Carl Hanser Publishers, Munich.
- Bonet, J., Lok, T.-S.L., 1999. Variational and momentum preservation aspects of smooth particle hydrodynamic formulations. *Comput. Methods Appl. Mech. Eng.* 180, 97–115. [http://dx.doi.org/10.1016/S0045-7825\(99\)00051-1](http://dx.doi.org/10.1016/S0045-7825(99)00051-1).
- Booy, M.L., 1978. Geometry of fully wiped twin-screw equipment. *Polym. Eng. Sci.* 18, 973–984.
- Breitenbach, J., 2002. Melt extrusion: from process to drug delivery technology. *Eur. J. Pharm. Biopharm.* 54, 107–117.
- Choulak, S., Couenne, F., Le Gorrec, Y., Jallut, C., Cassagnau, P., Michel, A., 2004. Generic dynamic model for simulation and control of reactive extrusion. *Ind. Eng. Chem. Res.* 43, 7373–7382.
- Cleary, P.W., Robinson, M., 2011. Understanding viscous fluid transport and mixing in a twin-screw extruder. In: *Proceedings of the 8th International Conference on CFD in Oil & Gas, Metallurgical and Process Industries*. Trondheim, Norway.
- Colagrossi, A., Bouscasse, B., Antuono, M., Marrone, S., 2012. Particle packing algorithm for SPH schemes. *Comput. Phys. Commun.* 183, 1641–1653. <http://dx.doi.org/10.1016/j.cpc.2012.02.032>.
- Conzen, C., 2008. Numerische und experimentelle Untersuchungen zu Transportvorgängen in Schneckenmaschinen. Kassel University Press, Kassel.
- Cummins, S.J., Rudman, M., 1999. An SPH projection method. *J. Comput. Phys.* 152, 584–607. <http://dx.doi.org/10.1006/jcph.1999.6246>.
- Durin, A., De Micheli, P., Nguyen, H.-C., David, C., Valette, R., Vergnes, B., 2014. Comparison between 1D and 3D approaches for twin-screw extrusion simulation. *Int. Polym. Process.* 29, 641–648.
- Eitzlmayr, A., Khinast, J., 2015. Co-rotating twin-screw extruders: detailed analysis of conveying elements based on smoothed particle hydrodynamics. Part 2: Mixing. *Chem. Eng. Sci.* (accepted for publication).
- Eitzlmayr, A., Koscher, G., Khinast, J., 2014a. A novel method for modeling of complex wall geometries in smoothed particle hydrodynamics. *Comput. Phys. Commun.* 185, 2436–2448. <http://dx.doi.org/10.1016/j.cpc.2014.05.014>.
- Eitzlmayr, A., Koscher, G., Reynolds, G., Huang, Z., Booth, J., Shering, P., Khinast, J., 2014b. Mechanistic modeling of modular co-rotating twin-screw extruders. *Int. J. Pharm.* 474, 157–176.
- Feldman, J., Bonet, J., 2007. Dynamic refinement and boundary contact forces in SPH with applications in fluid flow problems. *Int. J. Numer. Methods Eng.* 72, 295–324. <http://dx.doi.org/10.1002/nme>.
- Ficarella, A., Milanese, M., Laforgia, D., 2006a. Numerical study of the extrusion process in cereals production: Part I. Fluid-dynamic analysis of the extrusion system. *J. Food Eng.* 73, 103–111.
- Ficarella, A., Milanese, M., Laforgia, D., 2006b. Numerical study of the extrusion process in cereals production: Part II. Analysis of variance. *J. Food Eng.* 72, 179–188.
- Ghebre-Sellassie, I., Martin, C., 2003. *Pharmaceutical Extrusion Technology*. Marcel Dekker Inc., New York.
- Gomez-Gesteira, M., Rogers, B.D., Dalrymple, R.A., Crespo, A.J.C., 2010. Numerical simulation of interfacial flows by smoothed particle hydrodynamics. *J. Hydraul. Res.* 48, 6–27. <http://dx.doi.org/10.3826/jhr.2010.0012>.
- Grenier, N., Antuono, M., Colagrossi, A., Le Touzé, D., Alessandrini, B., 2009. An Hamiltonian interface SPH formulation for multi-fluid and free surface flows. *J. Comput. Phys.* 228, 8380–8393. <http://dx.doi.org/10.1016/j.jcp.2009.08.009>.
- Haghighyehi, R., Khalajzadeh, V., Farahani, M.F., Bahai, H., 2010. Experimental and CFD investigation on the solidification process in a co-rotating twin screw melt conditioner. *J. Mater. Process. Technol.* 210, 1464–1471. <http://dx.doi.org/10.1016/j.jmatprotec.2010.04.004>.
- Hétu, J.-F., Ilinca, F., 2013. Immersed boundary finite elements for 3D flow simulations in twin-screw extruders. *Comput. Fluids* 87, 2–11.
- Ihmsen, M., Cornelis, J., Solenthaler, B., Horvath, C., Teschner, M., 2014. Implicit incompressible SPH. *IEEE Trans. Vis. Comput. Graph.* 20, 426–435. <http://dx.doi.org/10.1109/TVCG.2013.105>.
- Ishikawa, T., 2001. 3-D non-isothermal flow field analysis and mixing performance evaluation of kneading blocks in a co-rotating twin screw extruder. *Polym. Eng. Sci.* 41, 840–849.
- Kalyon, D.M., Lawal, A., Yazici, R., Yaras, P., Railkar, S., 1999. Mathematical modeling and experimental studies of twin-screw extrusion of filled polymers. *Polym. Eng. Sci.* 39, 1139–1151.
- Kalyon, D.M., Malik, M., 2007. An integrated approach for numerical analysis of coupled flow and heat transfer in co-rotating twin screw extruders. *Int. Polym. Process.* 22, 293–302.
- Kleinebudde, P., 2011. Pharmazeutisches Produktdesign: Gezielte Freisetzung von Wirkstoffen durch unterschiedliche Extrusionstechniken. *Chem. Ing. Tech.* 83, 589–597. <http://dx.doi.org/10.1002/cite.201000162>.
- Kloss, C., Goniva, C., Hager, A., Amberger, S., Pirker, S., 2012. Models, algorithms and validation for opensource DEM and CFD-DEM. *Prog. Comput. Fluid Dyn. Int. J.* 12, 140–152.
- Kohlgrüber, K., 2008. *Co-Rotating Twin-Screw Extruders*. Carl Hanser Publishers, Munich.
- Kohlgrüber, K., Bierdel, M., Conzen, C., Hepperle, J., Kirchhoff, J., König, T., Thiele, H., 2012. Optimierter Betrieb und Scale-up von Doppelschnecken-Extrudern. In: *Seminar Handout. VDI Wissensforum, Leverkusen, Germany*.
- Kruisbrink, A.C.H., Pearce, F.R., Yue, T., Cliffe, K.A., H.P. Morvan, 2011. SPH concepts for continuous wall and pressure boundaries. In: *Proceedings of the 6th International SPHERIC Workshop. Schriftenreihe Schiffbau, Hamburg*.
- Lawal, A., Railkar, S., Kalyon, D.M., 1999. 3-D Analysis of Fully Flighted Screws of Co-Rotating Twin Screw Extruder. In: *SPE ANTEC Technical Papers*, pp. 317–321.
- Liu, G.-R., Liu, M.B., 2003. *Smoothed Particle Hydrodynamics: A Meshfree Particle Method*. World Scientific Publishing Co. Pte. Ltd., Singapore.
- Mahmood, O., Kassiotis, C., Violeau, D., Ferrand, M., Denis, C., 2011. Effect of wall boundary treatment in SPH for modelling turbulent flows with inlet/outlet. In: *Rung, T., Ulrich, C. (Eds.), 6th International SPHERIC Workshop. Schriftenreihe Schiffbau, Hamburg*, pp. 333–339.
- Malik, M., Kalyon, D.M., 2005. 3D finite element simulation of processing of generalized newtonian fluids in counter-rotating and tangential TSE and die combination. *Int. Polym. Process.* 20, 398–409.
- Malik, M., Kalyon, D.M., Golba, J.C., 2014. Simulation of co-rotating twin screw extrusion process subject to pressure-dependent wall slip at barrel and screw surfaces: 3D FEM analysis for combinations of forward- and reverse-conveying screw elements. *Int. Polym. Process.* 29, 51–62.
- Monaghan, J.J., 1989. On the problem of penetration in particle methods. *J. Comput. Phys.* 82, 1–15. [http://dx.doi.org/10.1016/0021-9991\(89\)90032-6](http://dx.doi.org/10.1016/0021-9991(89)90032-6).
- Monaghan, J.J., 1992. Smoothed particle hydrodynamics. *Annu. Rev. Astron. Astrophys.* 30, 543–574.
- Monaghan, J.J., 1994. Simulating free surface flows with SPH. *J. Comput. Phys.* 110, 339–406.
- Monaghan, J.J., 2000. SPH without a tensile instability. *J. Comput. Phys.* 159, 290–311. <http://dx.doi.org/10.1006/jcph.2000.6439>.
- Monaghan, J.J., 2005. Smoothed particle hydrodynamics. *Rep. Prog. Phys.* 68, 1703–1759. <http://dx.doi.org/10.1088/0034-4885/68/R01>.
- Monaghan, J.J., Kajtár, J.B., 2009. SPH particle boundary forces for arbitrary boundaries. *Comput. Phys. Commun.* 180, 1811–1820. <http://dx.doi.org/10.1016/j.cpc.2009.05.008>.
- Monaghan, J.J., Kos, A., 1999. Solitary waves on a Cretan beach. *J. Waterw. Port Coast. Ocean. Eng.* 125, 145–154.
- Morris, J.P., Fox, P.J., Zhu, Y., 1997. Modeling low Reynolds number incompressible flows using SPH. *J. Comput. Phys.* 136, 214–226. <http://dx.doi.org/10.1006/jcph.1997.5776>.
- Pawłowski, J., 1971. *Die Ähnlichkeitstheorie in der physikalisch-technischen Forschung*. Springer Publishers, Berlin/Heidelberg, Germany.
- Pokriefke, G., 2005. Numerische Analyse reibungsbehalteter Strömungen in teilgefüllten Extrudern. Universität der Bundeswehr, Hamburg.

- Potente, H., Bastian, M., Flecke, J., 1999. Design of a compounding extruder by means of the SIGMA Simulation Software. *Adv. Polym. Technol.* 18, 147–170. [http://dx.doi.org/10.1002/\(SICI\)1098-2329\(199922\)18:2<147::AID-ADV5>3.0.CO;2-X](http://dx.doi.org/10.1002/(SICI)1098-2329(199922)18:2<147::AID-ADV5>3.0.CO;2-X).
- Potente, H., Hanhart, W., 1994. Design and processing optimization of extruder screws. *Polym. Eng. Sci.* 3, 937–945.
- Potente, H., Kretschmer, K., 2002. Simulation and evaluation of compounding processes. *Macromol. Mater. Eng.* 287, 758–772. <http://dx.doi.org/10.1002/mame.200290005>.
- Pozorski, J., Wawrenczuk, A., 2002. SPH computation of incompressible viscous flows. *J. Theor. Appl. Mech.* 40, 917–937.
- Prat, L., Guiraud, P., Rigal, L., Gourdon, C., 2002. A one dimensional model for the prediction of extraction yields in a two phases modified twin-screw extruder. *Chem. Eng. Process.* 41, 743–751. [http://dx.doi.org/10.1016/S0255-2701\(02\)00003-X](http://dx.doi.org/10.1016/S0255-2701(02)00003-X).
- Price, D.J., 2012. Smoothed particle hydrodynamics and magnetohydrodynamics. *J. Comput. Phys.* 231, 759–794.
- Rathod, M.L., Kokini, J.L., 2013. Effect of mixer geometry and operating conditions on mixing efficiency of a non-Newtonian fluid in a twin screw mixer. *J. Food Eng.* 118, 256–265.
- Rauwendal, C., 2001. *Polymer Extrusion*, fourth ed. Hanser Publishers, Munich.
- Repka, M.A., Gutta, K., Prodduturi, S., Munjal, M., Stodghill, S.P., 2005. Characterization of cellulosic hot-melt extruded films containing lidocaine. *Eur. J. Pharm. Biopharm.* 59, 189–196.
- Rodríguez, E.O., 2009. Numerical simulations of reactive extrusion in twin screw extruders. Waterloo, Canada.
- Sarhangi Fard, A., Anderson, P.D., 2013. Simulation of distributive mixing inside mixing elements of co-rotating twin-screw extruders. *Comput. Fluids* 87, 79–91.
- Sarhangi Fard, A., Hulsén, M.A., Meijer, H.E.H., Famili, N.M.H., Anderson, P.D., 2012a. Adaptive non-conformal mesh refinement and extended finite element method for viscous flow inside complex moving geometries. *Int. J. Numer. Methods Fluids* 68, 1031–1052.
- Sarhangi Fard, A., Hulsén, M.A., Meijer, H.E.H., Famili, N.M.H., Anderson, P.D., 2012b. Tools to simulate distributive mixing in twin-screw extruders. *Macromol. Theory Simul.* 21, 217–240.
- Shao, S., Lo, E.Y.M., 2003. Incompressible SPH method for simulating Newtonian and non-Newtonian flows with a free surface. *Adv. Water Resour.* 26, 787–800. [http://dx.doi.org/10.1016/S0309-1708\(03\)00030-7](http://dx.doi.org/10.1016/S0309-1708(03)00030-7).
- Sobhani, H., Anderson, P.D., Meijer, H.E.H., Ghoreishy, M.H.R., Razavi-Nouri, M., 2013. Non-isothermal modeling of a non-Newtonian fluid flow in a twin screw extruder using the fictitious domain method. *Macromol. Theory Simul.* 22, 462–474. <http://dx.doi.org/10.1002/mats.201300110>.
- Teixeira, C., Gaspar-Cunha, A., Covas, J.A., 2012. Flow and heat transfer along the length of a co-rotating twin screw extruder. *Polym. Plast. Technol. Eng.* 51, 1567–1577.
- Vacondio, R., Rogers, B.D., Stansby, P.K., Mignosa, P., Feldman, J., 2013. Variable resolution for SPH: a dynamic particle coalescing and splitting scheme. *Comput. Methods Appl. Mech. Eng.* 256, 132–148. <http://dx.doi.org/10.1016/j.cma.2012.12.014>.
- Vergnes, B., Berzin, F., 2006. Modeling of reactive systems in twin-screw extrusion: challenges and applications. *Comptes Rendus Chim.* 9, 1409–1418. <http://dx.doi.org/10.1016/j.crci.2006.07.006>.
- Vergnes, B., Della Valle, G., Delamare, L., 1998. A global computer software for polymer flows in corotating twin screw extruders. *Polym. Eng. Sci.* 38, 1781–1792.
- Vyakaranam, K.V., Ashokan, B.K., Kokini, J.L., 2012. Evaluation of effect of paddle element stagger angle on the local velocity profiles in a twin-screw continuous mixer with viscous flow using Finite Element Method simulations. *J. Food Eng.* 108, 585–599. <http://dx.doi.org/10.1016/j.jfoodeng.2010.12.001>.
- White, J.L., Chen, Z., 1994. Simulation of non-isothermal flow in modular co-rotating twin screw extrusion. *Polym. Eng. Sci.* 34, 229–237.
- White, J.L., Kim, E.K., Keum, J.M., Jung, H.C., 2001. Modeling heat transfer in screw extrusion with special application to modular self-wiping co-rotating twin-screw extrusion. *Polym. Eng. Sci.* 41, 1448–1455.